Contents

List of Figures

List of Tables

1 Introduction

Optical pumping is a physical effect used to achieve population inversion. It was invented by Alfred Kastler who won the Nobel price in 1966 [1]. The method is commonly used in laser physics and made many precise measurements of nuclear spins and hyperfine structure splitting possible [2]. In this experiment, the method of optical pumping is demonstrated at the two isotopes ^{85}Rb and ^{87}Rb using circularly polarised light. The spectrum of the hyperfine structure of both isotopes is measured in the first part of the experiment, followed by the measurement of the nuclear spin of the two isotopes. Furthermore, the spin precession in the earth's magnetic field is observed and the strength of the earth's magnetic field is determined. Finally, the relaxation time of the pumped system is calculated using two different methods.

2 Theoretical background

This section provides a brief introduction to the theoretical background required for this experiment. Most of the information presented here is gained from reference [3], but it will be referenced in detail if something specific is taken from it. Apologizes are made, that the text inside some figures is in german, but this has happened since reference [3] was the best source for those pictures, which is written in german.

2.1 Hyperfine structure

In this experiment optical pumping is applied to the hyperfine structure (HFS) of ^{85}Rb and ^{87}Rb. The hyperfine splitting is caused by the interaction of the total angular momentum of the electron $\vec{J}$ with the nuclear spin $\vec{I}$. These two quantities couple to the total angular momentum $\vec{F}$ of the atom which is then given by

$$\vec{F} = \vec{I} + \vec{J}. \tag{1}$$

A sketch of this coupling is shown in Figure 1.

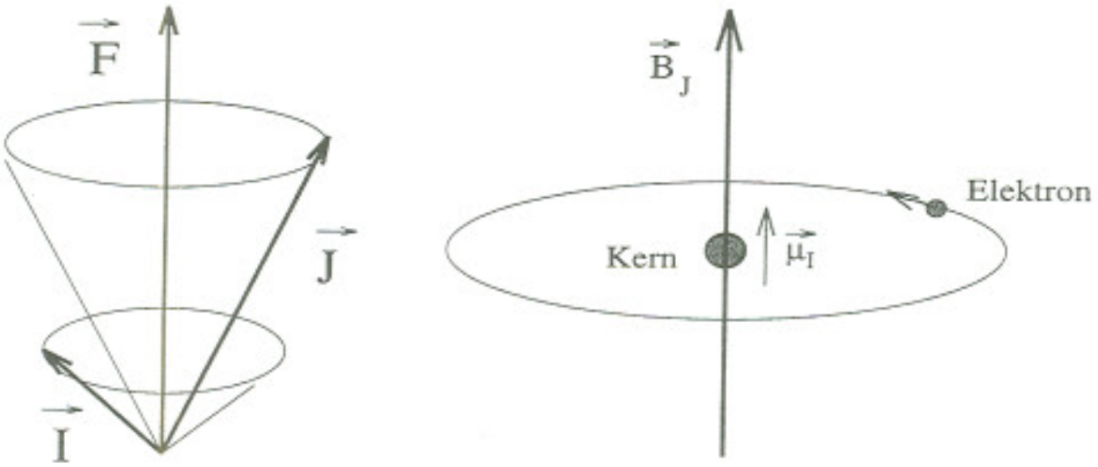

Figure 1: Sketch of the coupling of the total angular momentum $\vec{J}$ of the electron and the nuclear spin $\vec{I}$. This occurs due to the interaction between the magnetic field generated by the electron and the magnetic moment of the nucleus [3, p. 5].

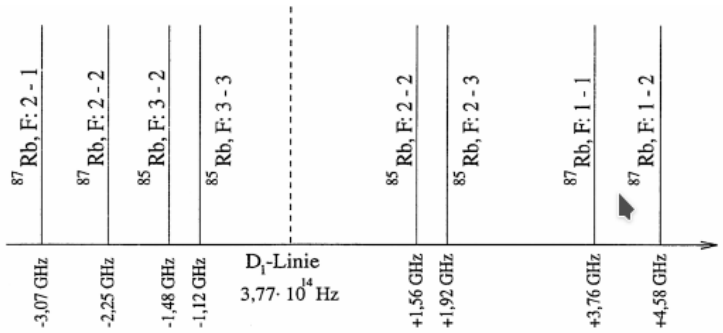

Figure 2: HFS-spectrum of the D1-line ($^2S_{1/2} \rightarrow {}^2P_{1/2}$) of ^{85}Rb and ^{87}Rb [3, p.12]. Each transition line is label with the F-quantum number from the lower state ($^2S_{1/2}$)) and the one from the upper state $^2P_{1/2}$. The dashed line in the middle is the line without taking HFS into account.

The mechanism is similar to the spin-orbit coupling, which is responsible for the fine structure where the electron's angular momentum $\vec{L}$ and the electron spin $\vec{S}$ add up to the total angular momentum of the electron $\vec{J}$. Similar to the quantum number J, F can only take the values within the range

$$|I - J| \leq F \leq I + J\,, \tag{2}$$

where the values proceed in integer steps. The energy splitting ΔE_{HFS} of the HFS is given by

$$\begin{aligned} \Delta E_{HFS} &= \frac{1}{2} \underbrace{\frac{g_I \mu_K B_J}{\sqrt{J(J+1)}}}_{=:A} [F(F+1) - I(I+1) - J(J+1)] \\ &= \frac{A}{2} [F(F+1) - I(I+1) - J(J+1)]\,, \end{aligned} \tag{3}$$

where g_I is the nuclear g-factor (analogue to the Landé-factor g_J of the fine structure), μ_K the nuclear magneton and B_J the magnetic field at the nucleus caused by the electron shell. The variable A defined in the above equation is called *interval constant*.

Since μ_K is approximately 3 orders of magnitudes smaller than the constant μ_S appearing in the fine structure, the resulting energy shifting of the hyperfine structure is also three orders of magnitude smaller then the energy shifting of the fine structure. Calculating the difference between two neighbouring energy levels of the hyperfine structure for constant I and J yields

$$\Delta E_{\Delta F=1}(F) = \Delta E_{HFS}(F+1) - \Delta E_{HFS}(F) = A(F+1). \tag{4}$$

By measuring the two frequencies $\nu(F+1)$ and $\nu(F)$ corresponding to the excitation energies $\Delta E_{HFS}(F+1)$ and $\Delta E_{HFS}(F)$, the interval constant can be calculated via

$$A = \frac{\Delta E_{\Delta F=1}(F)}{F+1} = \frac{\nu(F+1)\,h - \nu(F)\,h}{F+1} = \frac{\Delta \nu h}{F+1}, \tag{5}$$

where $\Delta\nu$ is the difference between the two frequencies $\nu(F+1)$ and $\nu(F)$ and h the Planck's constant. The HFS spectrum of the two isotopes ^{85}Rb and ^{87}Rb is shown in Figure 2.

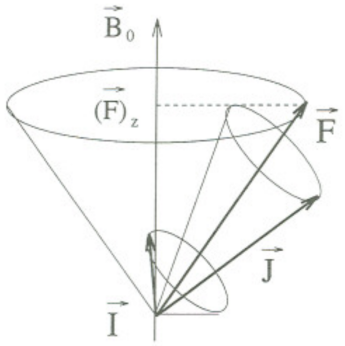

Figure 3: Schematic visualisation of the Zeeman effect. The total angular momentum of the atom precesses around the axis of the magnetic field [3, p. 16].

2.2 Zeeman effect of the hyperfine structure

Similar to the fine structure, there are $(2F+1)$ degenerated states with the same quantum number F but with different magnetic quantum numbers m_F, where

$$|-F| \leq m_F \leq F\,. \tag{6}$$

Applying a weak magnetic field B in the sense of

$$B \ll \frac{A}{g_J \mu_B}, \tag{7}$$

where g_J is the Landé-factor and μ_B the Bohr magneton, an additional energy splitting occurs, caused by the interaction of the external field with the total angular momentum of the atom F. The total angular momentum F starts to precess around the axis of the magnetic field as shown in Figure 3. The angular frequency ω_L of this precession in the external magnetic field B is given by

$$\omega_L = \frac{g_F\,\mu_B}{\hbar}\,B\,. \tag{8}$$

The energy of the atom is now depending on the alignment between $\vec{F}$ and the magnetic field which is described by the magnetic quantum number m_F. The resulting energy shift can be calculated using perturbation theory and is given by

$$E_B^{HFS} = g_F\,\mu_B\,B\,m_F\,. \tag{9}$$

For $J = \frac{1}{2}$ and therefore $F = I \pm \frac{1}{2}$ the energy difference between two neighbouring Zeeman levels levels is given by

$$\Delta E_B^{HFS}(\Delta m_F = 1) = \frac{g_J}{2(I+\frac{1}{2})}\mu_B B\,. \tag{10}$$

The full term diagram including the Zeeman levels can be seen in Figure 26 in the appendix.

2.3 Transitions in a multi level system

For simplicity only a two level system is discussed here, although the principles can be extended to a multi level system constisting of more than two states without any problems. The transition from one state to the other within a two level system can occur in three different ways. Electrons

from the lower energy state can interact with an external electric field by absorbing a photon of appropriate wavelength to get excited into the higher energy state. This process is called *stimulated absorption*. However, a photon of this specific wavelength can also cause an electron in the higher state to transition into the lower energy state by emitting a photon of the same energy, called *stimulated emission*. Furthermore, there is also the possibility to emit a photon randomly in order to transition to the lower energy state, which is called *spontaneous emission*.

These three mechanisms are accountable for the change of the population of states within a system. At thermal equilibrium, the distribution of the number of electrons in the higher energy level N_2 and the ones the lower energy level N_1 is given by the Boltzmann distribution

$$\frac{N_1}{N_2} = \frac{g_1}{g_2} \exp\left(-\frac{E_2 - E_1}{kT}\right). \tag{11}$$

Here, g_1 and g_2 are the degeneration of the states with the corresponding energy E_1 and E_2, which means that there are for example g_1 states with the same energy E_1, k is the Boltzmann constant and T the temperature [3].

For the Zeeman splitting of the HFS, the energy differences ($\approx 5 \cdot 10^{-28}\,\mathrm{J}$) are much smaller than kT (at $T = 300\,\mathrm{K}$: $kT \approx 5 \cdot 10^{-21}\,\mathrm{J}$). Therefore, the equilibrium population is approximately equally distributed among all Zeeman levels.

In order to describe the transition probabilities between different states of the multi level system, transition matrices can be used. A matrix element of such a transition matrix can be calculated depending on the external field [4, ch.15.3] by calculating

$$\left|\langle i|\hat{V}|j\rangle\right|^2, \tag{12}$$

where i, j are two quantum states and $\hat{V}$ is the operator of the external field. For linear polarised light this leads to the following selection rules for atomic transitions:

$$\begin{array}{llll} \Delta m_L = 0, & \Delta L = \pm 1, & \Delta n = \text{ arbitrary} & \text{fine structure} \\ \Delta m_F = 0, & \Delta F = \pm 1, & \Delta n = \text{ arbitrary} & \text{hyperfine structure} \end{array} \tag{13}$$

For circularly polarised light however, this leads to

$$\begin{array}{llll} \Delta m_L = \pm 1, & \Delta L = \pm 1, & \Delta n = \text{ arbitrary} & \text{fine structure} \\ \Delta m_F = \pm 1, & \Delta F = \pm 1, & \Delta n = \text{ arbitrary} & \text{hyperfine structure} \end{array} \tag{14}$$

2.3.1 Line width

In general, the uncertainty principle makes it impossible to generate a photon with an exact frequency. This would correspond to an infinitely spread wave. There is always a so called *natural line width* of the frequency, depending on the lifetime of a transition. The shorter the lifetime, the larger the natural line width. The frequency curve is gaussian shaped around the expectation value.

In practice there are two more mechanism which broaden the frequency spectrum. One is the *Doppler broadening*, caused by the relative motions of the atoms. If an atom flies towards a detector, then the frequency of emitted photons are higher and vice versa.
The second mechanism is called *pressure broadening*. Higher pressure is accountable for more atomic collisions within a system. These collisions cause a phase shift of the atoms whereby an additional broadening can occur.

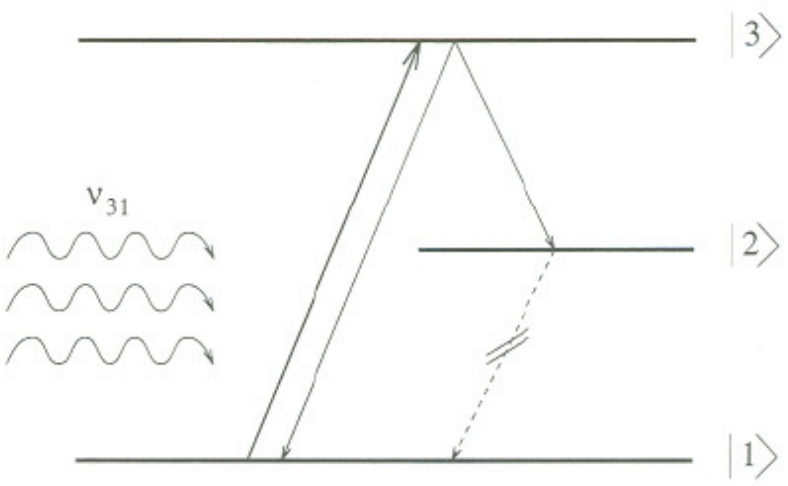

Figure 4: Sketch of the principle of optical pumping [3, p.27]. Electrons in $|3\rangle$, transitioned from $|1\rangle$ have a probability to transition to $|2\rangle$ via spontaneous emission. From here they can not come back to $|1\rangle$. After a little time a certain amount of electrons is pumped into $|2\rangle$.

2.4 Optical pumping

The goal of optical pumping is to generate a population of states which is different to the population of states in the equilibrium case. This is widely used for lasers, where optical pumping generates a population inversion, i.e. the state with higher energy is more populated than the one with lower energy. Therefore, the electrons are "pumped" into a specific state.

The simplest case is drawn in Figure 4. Assuming we have a three level system with levels $|1\rangle$, $|2\rangle$ and $|3\rangle$. If laser light of the frequency ν_{31} corresponding to the energy difference between $|1\rangle$ and $|3\rangle$ is shined in, stimulated absorption occurs in the system, lifting electrons from $|1\rangle$ to $|3\rangle$. On $|3\rangle$, the electrons can transition to $|1\rangle$ back again or transition to $|2\rangle$ with a certain probability. Once in state $|2\rangle$, the electrons have no chance to get to another level of the system. To get to $|3\rangle$, there is the need of light with frequency ν_{32}. Due to selection rules, electrons can not transition from state $|2\rangle$ to $|1\rangle$. As a result of that, the electrons are so to say stuck in that state, which is why the number of electrons in state $|2\rangle$ can be increased significantly with optical pumping.

In the experiment there are some processes, that work against the optical pumping by changing the population towards the lower state again. These are called *relaxation processes* and are discussed later in more detail. In general, this leads to the fact that not every electron can be pumped into the higher level. Instead, there is an equilibrium when the changing rate of states for both processes cancel each other out. When N_+ is the number of electrons in the higher level and N_- in the lower level, then the difference $n(t)$ between them can be calculated with

$$n(t) = N_+(t) - N_-(t) = (n_0 - n_{max}) \exp\left(-\frac{t}{\tau}\right) + n_{max}, \tag{15}$$

with $n_0 = n(t = 0)$, the maximum difference n_{max}, the time t and a time constant τ. The time constant τ can furthermore be expressed as

$$\frac{1}{\tau} = \frac{1}{T_P} + \frac{1}{T_R}, \tag{16}$$

where T_P is a time constant regarding the pumping process, called *pumping time*, and T_R a time

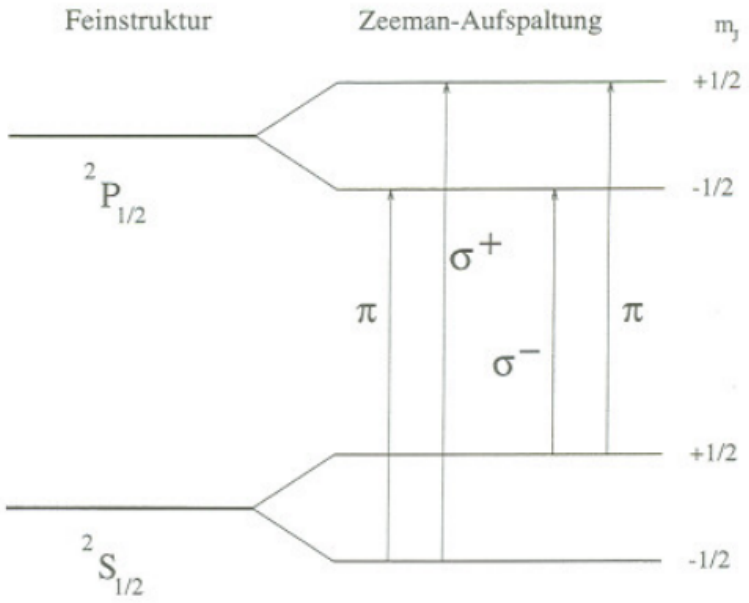

Figure 5: D1-transition ($^2S_{1/2} \rightarrow {}^2P_{1/2}$) of Rubidium. The transition from the different Zeeman levels are only possible with light with certain polarisations. The transitions with $\Delta m_J = 0$ can only be done with linear polarised light (π-light), whereas the transition with $\Delta m_J = \pm 1$ are done with circularly polarised light ($\sigma^{\pm}$-light)

constant regarding the relaxation processes, called *relaxation time*.

2.4.1 Optical pumping of Rubidium

Since the hyperfine structure leads to very many different Zeeman levels, the explanation of the optical pumping of Rubidium is done for the case of the fine structure here. The different Zeeman levels and the possible transitions between them are shown in Figure 5. As indicated in Figure 5, different transitions correspond to different polarisations of light. While transitions without a change in the magnetic quantum number ($\Delta m_J = 0$) correspond to linearly polarised light, transitions which change the magnetic quantum number of the electron ($\Delta m_J = \pm 1$) correspond to circularly polarised light.

Therefore, to realise optical pumping in the case of the Rubidium D1-line, circularly polarised light is used. In this section, the Zeeman levels are referred to as $S(+1/2)$, $S(-1/2)$, $P(+1/2)$, and $P(-1/2)$. As described in subsection 2.3, the thermal equilibrium state of the Zeeman levels of $^2S_{1/2}$ is approximately at $N_{m_j=+1/2} = N_{m_j=-1/2}$. If a cell containing Rb-gas is exposed to right handed circularly polarised light (σ^+-light), the electrons in the state $S(-1/2)$ are excited into the $P(-1/2)$-level by the absorption of a photon. From here, they have a transition probability of 2/3 to go back into the old $S(-1/2)$ level again but with 1/3 probability they can transition to the $S(+1/2)$ level. Once they are in this level, they can not absorb any more σ^+ light to get excited into a higher state, nor can they transition into the lower state due to selection rules. The electrons are trapped in this level and pumping is possible. Due to reasons of symmetry, using linearly polarised light would not change the population numbers of the different energy levels, which is why optical pumping is not possible with linearly polarised light in this case.

The electrons in $S(+1/2)$ are aligned parallel to the external magnetic field, while electrons in $S(-1/2)$ are aligned anti parallel. If there are more particles in a certain state due to the optical

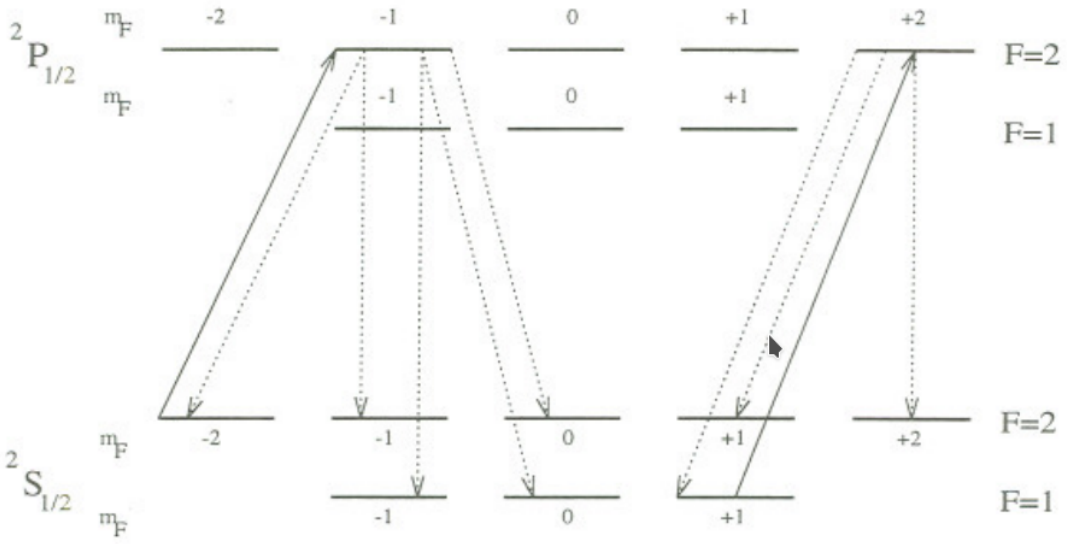

Figure 6: Pumping the D1-line of ^{87}Rb. Every time a circularly polarised photon is absorbed, the quantum number m_F is increased by one. Then there are several ways to go back to a lower level, but only one channel lowers m_F back again. So in general the distribution gets shifted towards a higher m_F number until most of them are in $m_F = 2$.

pumping process, the whole system becomes polarised. This is used for measuring the time that is needed for pumping. If for example the direction of the magnetic field is switched, the population of states is switched as well and pumping can begin again. This will be explained in more detail in subsubsection 3.2.5.

A sketch of the possible states and transitions in the case of optical pumping of the Zeeman levels of ^{87}Rb can be seen in Figure 6. The nucleus of ^{87}Rb has a nuclear spin of $I = 3/2$ and both electron states that are examined here have a total angular momentum of $J = 1/2$. Therefore, there are 8 hyperfine states for both $^2S_{1/2}$ and $^2P_{1/2}$, 3 with $F = 1$ with $m_F \in [-1, 1]$ and 5 in $F = 2$ with $m_F \in [-2, 2]$. If a right handed circularly polarised photon is absorbed, the magnetic quantum number m_F is increased by one due to conservation of angular momentum. As a result of that, the population gets shifted towards a higher number of m_F in general, causing a higher polarisation. Therefore, many electrons populate the state $^2S_{1/2}$, $F = 2$, $m_F = 2$. Analogously, the mainly populated state in the case of optical pumping of the ^{85}Rb isotope is $^2S_{1/2}$, $F = 3$, $m_F = 3$.

2.5 Relaxation processes

The relaxation of Rb-isotopes is primarily governed by the interactions with other atoms. Hence energy can get lost, whereas this is not possible by the interaction with a radiation field, since the needed transitions is forbidden.

In this experiment, the Rb-isotopes are in a cell of glass. Collisions of the Rb-isotopes with the glass are one relaxation process. The other process are the collisions between two Rb-isotopes, which can also cause an energy loss for one isotope. Both processes can be slowed down by introducing a puffer gas in the cell with which the Rb-isotopes are not able to interact, reducing the number of occurring relaxation processes. These puffer gases are noble gases in general. Getting a long relaxation time is not a trivial task and depends on several parameters. These are the choice of the element, the dimension and shape of the cell as well as the pressure applied to the cell.

For a spherical cell, the inverse longitudinal relaxation time T_D can be calculated with

$$\frac{1}{T_D} = \frac{D_0 p_0}{p} \left(\frac{2\pi}{d}\right)^2 , \tag{17}$$

where D_0 is the diffusion coefficient at a certain pressure p_0, p the applied cell pressure and d the diameter of the cell body. Using the values $p_0 = 101.3\,\text{kPa}$, $p = 150\,\text{Pa}$, $D_0 = 0.16\,\text{cm}^2/\text{s}$ and $d = 5\,\text{cm}$ given in [5, p.7, p.21] yields the value

$$T_D = 5.9\,\text{ms}\,. \tag{18}$$

3 Experimental setup and execution

This section provides a description of the experimental setup used for the different parts of the experiment. Furthermore, the execution and the used methods are briefly explained. The handwritten notes which are taken during the experiment can be found in Figure 37 - Figure 39 in the appendix.

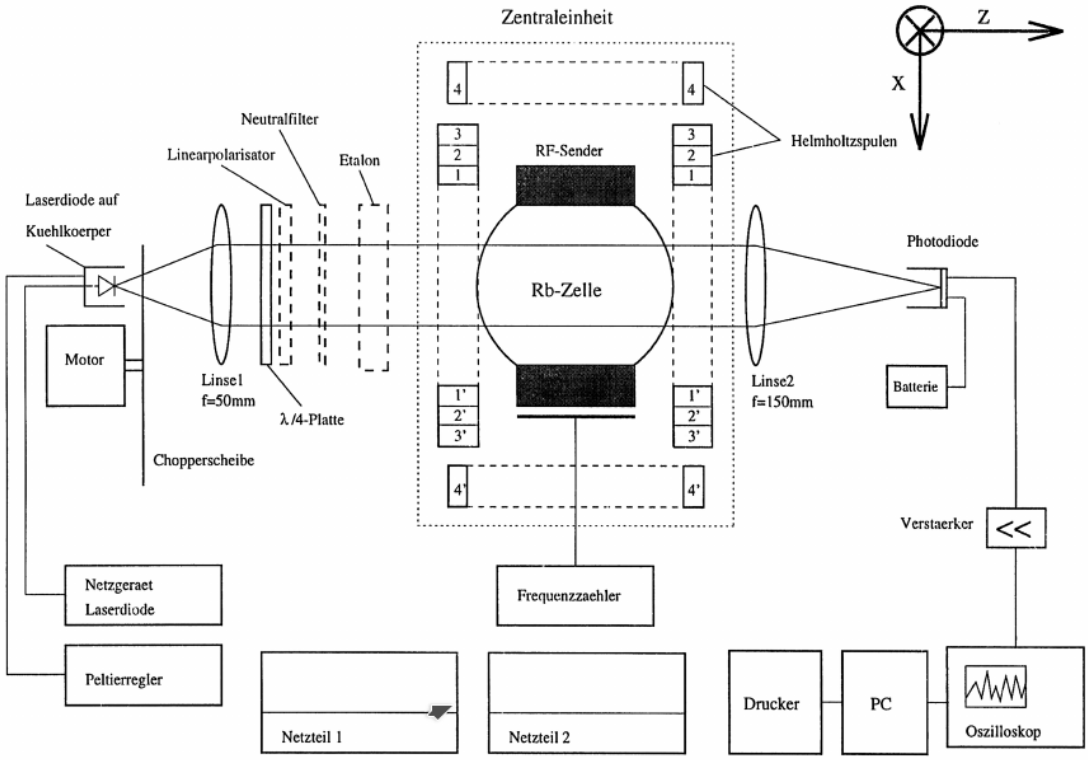

Figure 7: Overview of the whole optical pumping setup. Details about each component can be found in reference [5, p.9].

3.1 Setup

An overview of the whole setup can be found in Figure 7. The general setup consists of a beam line consisting of a laser diode, two lenses for the alignment of the beam, a glass cell filled with gas of Rubidium, in the following called *Rb-cell*, and a photodiode which detects the signal of the transmitted light. Around the Rb-cell, there are four different coils which are later used to create and compensate different magnetic fields. Components like a quarter-wave-plate, a linear

polariser, a etalon and different kinds of neutral filters are inserted in the beam line in different parts of the experiment, which are discussed in more detail in the following.

For later parts of the experiment, there is also a chopper, which can be used to block the laser beam as well as an radio frequency radiation emitter. The signals of the photodiode and the magnetic fields are visualised with an oscilloscope. The photodiode, which is used to measure the transmission signal, is preamplified by a 9 V battery to avoid long rising times [5, p.7]. Furthermore, several power supplies and frequency generators are provided for the laser diode and the different coils.

3.1.1 Laser diode and the beam line

The light source used in this experiment is a semiconductor laser diode. The frequency of the emitted light can be adjusted with two parameters, namely the temperature of the diode and the current of the power supply. The temperature is controlled by a so-called Peltier element which is able to control the temperature of the diode within the range 30 °C - 40 °C. The power supply can provide a current up to 100 mA, but the laser is at most driven at 80 mA, because otherwise the laser is aging more quickly and gets slowly destroyed.

Changes in either of these two parameters lead to a change in the gap with of the diode, which then leads to a change in the energy of the emitted photons. By increasing the current in the diode the frequency of the emitted light is approximately decreasing linearly in certain intervals [3, p.62]. Due to thermal effects, leaps in the frequency can occur between these intervals, which can be seen in Figure 8. This effect is called *mode hopping*. In this report, the combination of the two laser parameters (temperature and current) is called *working point*. These working points vary between different measurements since these are performed on different days.

For some parts of this experiment, the laser frequency has to be varied over a specific interval within a short period of time. In order to obtain a linear relation between the current of the laser diode and the frequency of the emitted light, the corresponding interval of the current has to be chosen in a way that there are no mode hoppings taking place within the chosen interval.

To optimize the beam path, there are two lenses available. The laser light is focused by the first lense, creating a parallel beam. A second lens after the Rb-cell focuses the beam onto the photodiode.

3.1.2 Etalon

In order to measure the frequency of the laser light an etalon is used in the first part of the experiment. A sketch of an etalon is shown in Figure 9. The etalon is a glass plate of which the front and back side are partially mirrored. The result of these partially mirrored planes is that the incident light gets partially reflected at the transitions between the glass and the air. Therefore, if the light gets reflected twice in the etalon as shown in the sketch, the beam interferes with itself, resulting in either constructive or destructive interference. If the laser beam is perpendicular to the glass of the etalon, the criteria for constructive interference and therefore a transmission maximum is given by

$$\lambda = \frac{2\,d\,n}{m}\,, \tag{19}$$

where λ is the wavelength of the laser light, d is the thickness of the etalon, n is the refractive index of the etalon's material and m is an integer number corresponding to the order of the maximum. Rearranging this formula for the frequency of the laser light leads to

$$\nu(m) = \frac{c}{\lambda} = \frac{c\,m}{2\,n\,d}\,, \tag{20}$$

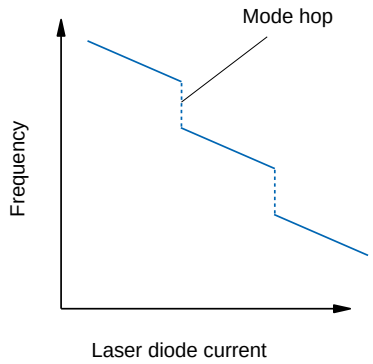

Figure 8: Mode hopping of the laser diode. Scaling and units are arbitrary. If the energy of the gap width and thus the frequency of emitted photons is increased by changing the current in the diode. At a certain level mode hopping occurs, which are the non-linear leaks in the graph, can occur due to thermal effects of the diode by changing either the current or the temperature of the diode. A comparable plot can be found in [6, p.6].

where c is the speed of light in vacuum. The frequency difference between two neighbouring frequencies that satisfy Equation 20 is then given by

$$\delta\nu = \frac{c}{2\,n\,d}\,. \tag{21}$$

This parameter is called the *free spectral range* (FSR) and the corresponding value of the etalon used in this experiment is $\delta\nu = (9924 \pm 30)\,\mathrm{MHz}$ [3, p. 52].

3.1.3 Neutral filters, polarisers and quarter wave plate

In this experiment, right handed circularly polarised light is needed for the optical pumping process. This is generated by a quarter wave plate. The light emitted by the laser diode is already linear polarised light. If the polarisation vector is viewed in the two dimensional space, it can be described by two orthogonal basis vectors. A quarter wave plate changes the relative phase between the two basis vectors, causing the polarisation vector to rotate. A linear polarisation filter after the quarter wave plate is then used for checking if the light is indeed right handed circularly polarised. If this is the case, the measured transmitted intensity stays the same among all angles of the linear polarisation filter.

In order to weaken the light intensity without changing the polarisation, neutral filter are used. These are characterized by the optical density D, which is given by

$$D = -\log_{10}\left(\frac{I}{I_0}\right), \tag{22}$$

where I is the intensity after the neutral filter and I_0 the intensity without any filter [5, p.7]. The transmittance, which is the relative intensity x is therefore

$$x = I/I_0 = 10^{-D}\,. \tag{23}$$

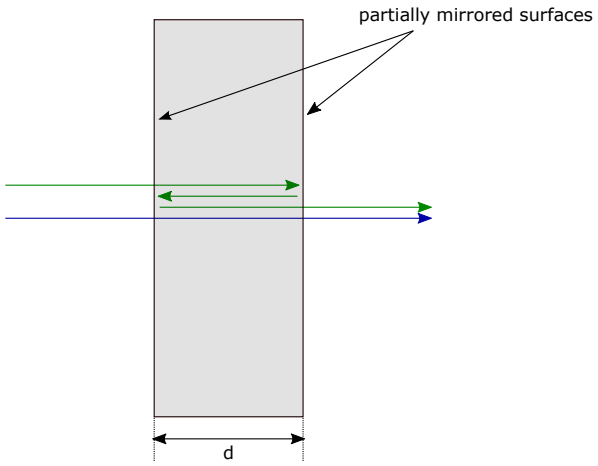

Figure 9: Schematic representation of an etalon. The green and the blue lines are both part of the incident light beam. While the blue beam passes both surfaces without any reflection, the green beam is reflected two times in the etalon. The blue and the green beam interfere after the etalon, leading to constructive or destructive interference depending on the path difference between the two beams. Note that the green lines after the reflection are only shifted slightly for the purpose of visibility. In reality, these lines are all on top of each other.

3.1.4 Rubidium cell

The heart of the experiment is the Rb-cell. It is a spherical glass object with $\approx 5\,\text{cm}$ diameter, filled with the natural ratio of the isotopes ^{85}Rb (72.8%) and ^{87}Rb (27.2%) [5, p.7]. To encounter the relaxation processes, the cell is filled with Krypton as a puffer gas with a pressure of $\approx 150\,\text{Pa}$ at room temperature. Temperature and pressure can be changed by using a professional hair dryer in order to get a better signal.

Build upon the cell, there a a radio frequency emitter (RF emitter). This is later used for inducing transitions between Zeeman levels of the HFS structure. It can be tuned around a frequency of 500 KHz.

3.1.5 Helmholtz coils for the magnetic fields

To adjust the magnetic field, there are 5 different Helmholtz coils. The coil parameters can be found in Coil 1 and 2 in Figure 7 are in horizontal position. Coil 1 is used to get a constant magnetic field while coil 2 is able to vary the magnetic field by a certain shape, in this case a sinus function. Coil 3 has a small number of windings in order to be able to switch the magnetic field fast because of the low inductivity. Coil 4 is used to create a a constant magnetic field in vertical direction. Another coil with only 5 windings, coil number 5, which is attached to the Rb-cell but is not shown in Figure 7, also has low inductivity. The conversion factors listed in 1 correspond to the formula

$$\begin{aligned} B = \mu_0 H &\approx 0.7155 \mu_0 \frac{n}{r} I \\ \iff \frac{B}{I} &\approx 0.7155 \mu_0 \frac{n}{r} \end{aligned} \tag{24}$$

Table 1: Coil parameters. Coil 1, 2, 3 are the horizontal ones, coil 4 the vertical one which can also be found in Figure 7 [5, p.8].

Coil number	Windings	Diameter [m]	$k = \frac{B}{I}$ (theo.) $[\frac{\text{Vs}}{\text{Am}^2}]$	$k = \frac{B}{I}$ (measured) $[\frac{\text{Vs}}{\text{Am}^2}]$
1	80	0.09	$7.99 \cdot 10^{-4}$	$(7.99 \pm 0.01) \cdot 10^{-4}$
2	80	0.09	$7.99 \cdot 10^{-4}$	$(8.14 \pm 0.01) \cdot 10^{-4}$
3	5	≈ 0.09	$1.00 \cdot 10^{-4}$	-
4	60	0.246	$4.38 \cdot 10^{-4}$	$4.76 \cdot 10^{-4}$

3.2 Execution and methods

In this subsection, the execution of the different parts of the experiment and the used methods are explained.

3.2.1 Laser characterisation

In order to characterise the laser diode and to find an appropriate working point for later measurements, several measurements are performed. These measurements are done without the Rb-cell but with the etalon in the beam line. The current applied to the laser diode is the sum of a constant offset and a triangular shaped current. Several temperatures and diode currents are tested in order to observe the relation between the frequency of the laser and these parameters. Furthermore, this is done in order to ensure that the working point used for the measurement of the HFS spectrum does not show mode hopping.

3.2.2 HFS spectrum of the D1-line of Rb

The general idea behind this method is that if the laser frequency matches a certain HFS transition, part of the photons will be absorbed and therefore the intensity of the transmission signal is reduced. For this measurement only the two lenses and the Rb-cell are placed in the beam path. Furthermore, a laser frequency gauge is made with the etalon.

Around the working point determined in the laser characterisation, the current of the laser diode is then increased and thus the frequency decreased linearly in order to go through the HFS spectrum, resulting in a drop of the transmission signal at the HFS lines. In this experiment, a triangular function is used for the current of the laser diode, which results in a positive and negative slope of the intensity, each showing the whole HFS spectrum. An exemplary plot can be seen in Figure 10a. The change of the laser frequency with respect to the change in time can be determined using the etalon described in subsubsection 3.1.2. For this gauge, the same ramping is applied to the laser as used in taking the HFS spectrum later on, but with the etalon and without the Rb-cell in the beam path. Since the difference in frequency between two etalon peaks is a known quantity (see subsubsection 3.1.2), a conversion factor between time and frequency can be calculated. To be more specific, only the change in frequency can be assigned, not the actual real frequency, since there is an unknown offset. However, in this case only differences in frequencies are relevant, which is why this is not a problem.

Since the ramping of the current is not symmetrical, the evaluation has to be made for both ramping up and ramping down seperately. Furthermore, the parameters of the ramping are chosen equally for measuring the HFS spectrum as well as the current-frequency gauge. This way, it is

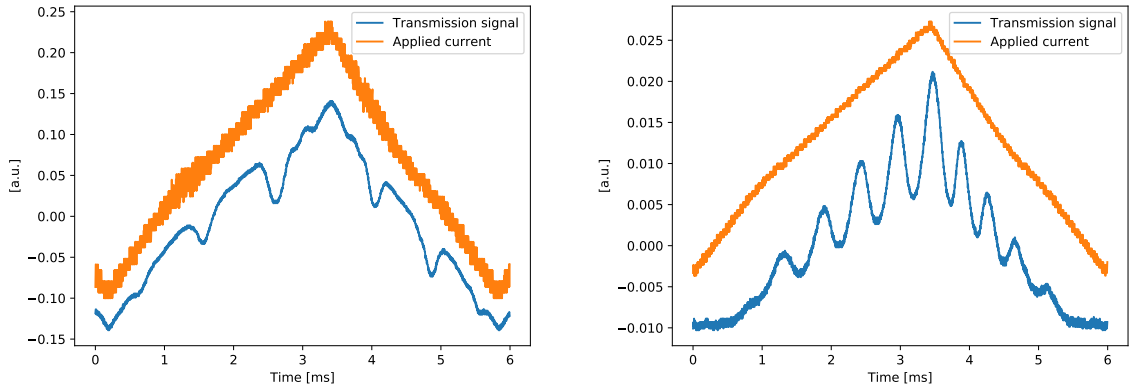

(a) **(b)**

Figure 10: Measurement of the HFS spectrum. The blue curve shows the transmission signal recorded by the photodiode, while the orange curve shows the ramping of the current. The vertical axis of both graphs are scaled arbitrarily in order to make them visible in the same plot. Remember that the intensity is increasing, frequency is decreasing, when the current is ramped up. Vice versa when the current is ramped down on the right flank. On the left hand side in **(a)**, a example plot of the HFS spectrum is shown. Six out of eight possible absorption lines are visible per ramping. On the right hand side **(b)**, the frequency gauge is shown. The peaks from the constructive interference are visible in a equidistant way. With the distance between them the frequency gauge can be determined.

made sure that no mode hopping occurs and the assumption that the frequency changes linearly with the current is viable.

The assignment of the peaks to the respective transitions can then be made with the spectral lines shown in Figure 2. This can be done by a visual comparison of how the peaks look like here with the actual data taken.

Now the energy difference between the hyperfine splitting of a fine structure state is given by the differences of the frequencies of two transitions with a difference in F of $\Delta F = 1$. The result of this should either give the hyperfine splitting of the state $^2S_{1/2}$ or $^2P_{1/2}$. This is sketched in Figure 11. Thus the interval constant A can be calculated with Equation 5.

3.2.3 Double resonance

In this part of the experiment, the strength of the earths magnetic field as well as the nuclear spin of the two Rb isotopes are calculated. This is done by using the principle of *double resonance*. Using a constant magnetic field in coil number 1, the energy levels of the Rb isotopes are split according to the Zeeman effect as explained in subsection 2.2. Using optical pumping, there is a significant deviation of the occupation numbers compared to the occupation numbers of the equilibrium state.

In the ideal case, all atoms of the ground state would be pumped into the higher energy state where the electrons are trapped. This would mean that the laser light, which is used for the optical pumping is not absorbed at all, resulting in maximal transparency of the cell. In order to redistribute the occupation numbers, and to allow transitions working against the pumping process, radio frequency radiation is used.

If the energy of the RF-photons matches the energy between the Zeeman levels, induced emission can occur, resulting in more atoms occupying the ground state. Subsequently, the transparency of the Rb-cell decreases, since there are now more atoms in the cell that can be pumped again.

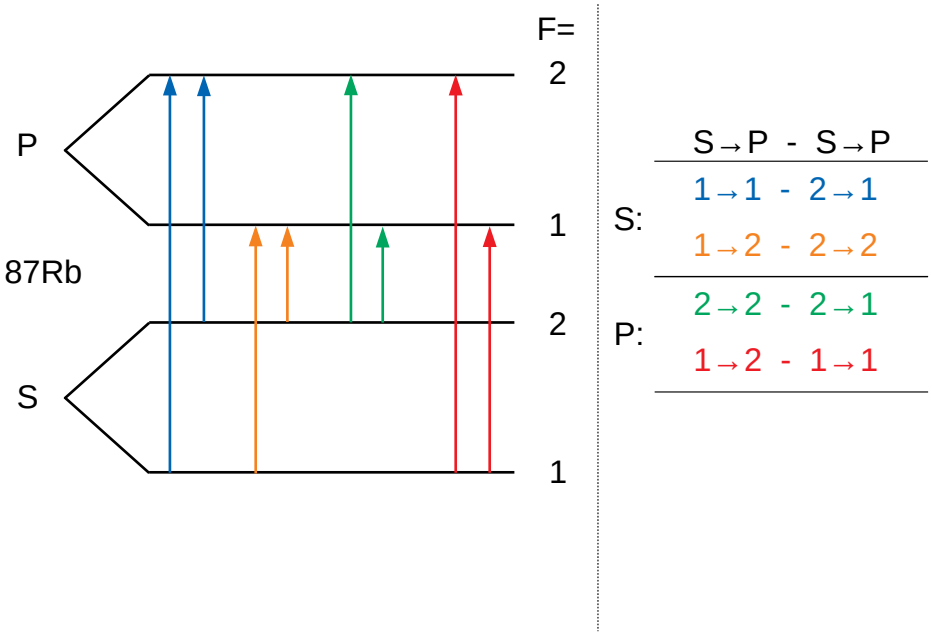

Figure 11: Calculating the energy differences $\Delta E_{HFS}(F+1) - \Delta E_{HFS}(F)$ of the hyperfine splitting for ^{87}Rb. The differences of each pair of arrows is equal to the hyperfine splitting of either $^2S_{1/2}$ or $^2S_{1/2}$. The same can be applied to ^{85}Rb by rasing all quantum numbers of F by one.

In order to tune the constant magnetic field leading to the energy splitting corresponding to the incident radiation, several adjustments of the magnetic fields are performed, while the RF-radiation is kept at a constant frequency of approximately 500 kHz.

To compensate the vertical component of the earth's magnetic field, a constant current is applied in coil number 4, until the intensity of the absorption peaks is maximal. Afterwards, a sinusoidal magnetic field is created with coil number 2 in horizontal direction. In the same direction as the magnetic field of coil number 2, a constant magnetic field is applied with coil number 1. The current of coil number 1 is adjusted in order to observe equidistant peaks in the signal. If this is the case, then the energy of the Zeeman splitting created by the constant magnetic field in horizontal direction (coil number 1 and earth's magnetic field) is equal to the energy of the RF photons. Using the information of the different applied magnetic fields, the earth's magnetic field as well as the nuclear spin of the Rb isotopes is calculated, which is explained in more detail later in the analysis in subsection 4.3.

3.2.4 Spin precession

As previously mentioned in subsection 2.2, spin precession or in the case of I-J-coupling the precession of the total angular momentum vector can occur when applying an external magnetic field. This effect is used in this experiment in order to determine the strength of the earths magnetic field. By applying an external field and using optical pumping, the spins of the atoms in the system are aligned along the external field.

In this part of the experiment, the horizontal component of the earth's magnetic field is compensated by applying the corresponding current obtained in the double resonance measurement. Furthermore, coil number 5 is connected to a rectangular current signal. As a result of that, the spins are aligned along the magnetic field of coil number 5 when the current signal is non-zero.

When this external field is switched off within a shorter time period than the timescale of the spin precession in the earths magnetic field, this precession can be observed. Using Equation 8, the vertical component of the earth's magnetic field can then be calculated.

3.2.5 Measurement of the relaxation time using the Dehmelt method

This method uses the behaviour of the pumped system after changing the direction of the magnetic field. Optical pumping aligns the spins of the Rubidium atoms along the magnetic field. At the same time, relaxation processes as explained in subsection 2.5 are reducing the number of electrons in the pumped state. Once the system is pumped long enough, there is an equilibrium point where the number of atoms leaving the overpopulated state due to relaxation is equal to the number of atoms which are pumped into that state. The result of this equilibrium is a constant transparency of the Rb cell in the laser beam.

The earth's magnetic field is compensated using coil number 1 (horizontal component) and coil number 4 (vertical component). An alternating rectangular current which changes the sign after a specific period is applied to coil number 3, resulting in an alternating magnetic field. When reversing the direction of the magnetic field, the sign of the magnetic quantum number m_F is getting flipped as well, which leads to the situation where pumping is possible again. Therefore, the resulting absorption signal has a negative peak right after the point in time at which the B-field direction is changed. Afterwards, the transparency increases again following an exponential curve as shown in Equation 15. As both pumping and relaxation processes are happening during that time, the timescale τ of that exponential increase, which was introduced in Equation 16, is given by

$$\frac{1}{\tau} = \frac{1}{T_P} + \frac{1}{T_R}\,, \tag{25}$$

where T_P is the pumping time and T_R the relaxation time. Since the pumping time is inversely proportional to the intensity of the laser light I_{light},

$$T_P \propto \frac{1}{I_{\text{light}}}\,, \tag{26}$$

Equation 25 can be written as a linear function of the intensity

$$\frac{1}{\tau} = \frac{1}{T_R} + b \cdot I_{\text{light}}\,, \tag{27}$$

where b is a constant factor. Using this linear relation between the inverse of the orientation time τ and the intensity of the laser light, the relaxation time T_R can be determined by calculating the value of $1/\tau$ for different laser intensities and afterwards applying a linear fit to these values. The inverse of the relaxation time is then given by the offset of the linear fit.

In this experiment, several neutral filters are used in order to obtain the orientation time for different values of the laser intensity. The values of $1/\tau$ are determined by performing an exponential fit. The resulting values are then plotted as a function of the relative intensity in order to perform the linear fit explained above.

3.2.6 Measurement of the relaxation time using the Franzen method

With Franzens method to determine the relaxation time, one uses the fact that the intensity of the transmitted light is exponentially decreasing when the pumping process is turned off. Here no special magnetic field is required. The shut down of the pumping is simply done by blocking the laser with the chopper wheel. The more time passes the more the system has relaxed. Therefore,

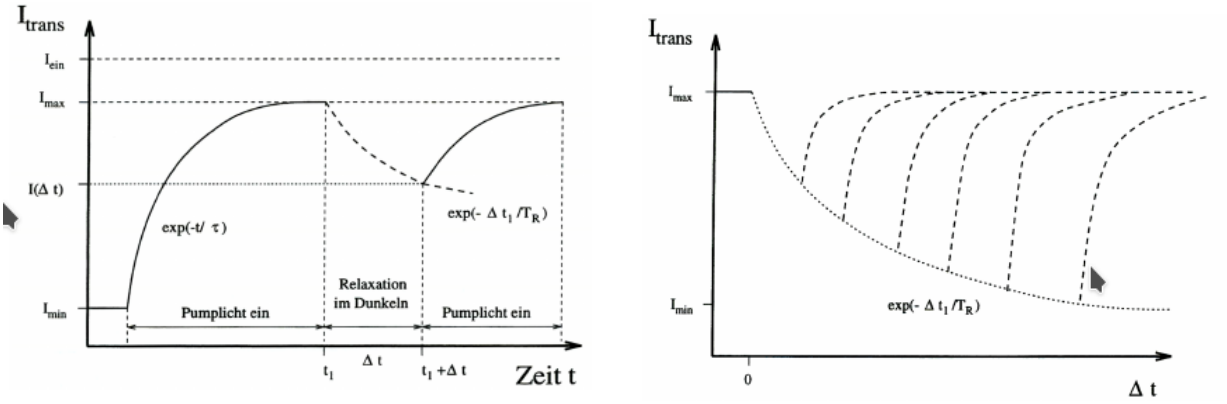

(a) **(b)**

Figure 12: Relaxation with blocking the laser. While pumping is active, the transmitted light converges to a maximum value I_{max} quickly (within <2ms). When the laser is blocked, only the relaxation processes are active anymore and the transmitted light decreases exponentially until the laser can shine in again **(a)**. The initial values of the intensity curves when the laser shines in again build the desired relaxation curve **(b)**. (From [3, p.88], [5, p.22])

more absorption is possible again and the intensity of the transmitted light is lower. The intensity follows a curve of the form

$$I(\Delta t) = I_{min} + (I_{max} - I_{min}) \cdot \exp -\frac{\Delta t}{T_R}. \tag{28}$$

The problem with this is, that the intensity curve can not be measured directly, since the laser is blocked and there is no transmitted light whatsoever. So the idea is to measure the intensity of the laser right after the signal is back on. This is done for different time intervals Δt in which the system can relax. When the cell is exposed to the laser light again, there can be seen an exponential increase with different starting values. Depending on how long the laser was blocked (*dark time*), this curve starts at a different value, whereas the value is lower for longer dark times. The first value of this curve represents the intensity of the desired curve at a certain relaxation time Δt, which can be seen in Figure 12. With several intensities $I_{trans}(\Delta t)$ at different Δt an exponential fit can be performed to determine the parameter of the relaxation time T_R.

4 Analysis

In this analysis, the uncertainty of a quantity x is called s_x. All uncertainties are calculated via gaussian error propagation. This means that the uncertainty s_x of the quantity $x(y, z)$ which depends on the variables y and z is calculated with

$$s_z = \sqrt{\left(\frac{\partial x}{\partial y}\, sy\right)^2 + \left(\frac{\partial x}{\partial z}\, s_z\right)^2}. \tag{29}$$

The correlation between the quantities are assumed to be negligible throughout the protocol.

4.1 Characterisation of the laser diode

In order to characterise the laser diode several measurements are performed without the Rb-cell but with the etalon in the beam path. The current applied to the laser diode is a constant offset

I_{diode} in addition with a triangular shaped signal. This technique allows to visualise the change of the laser's frequency with the change of the current. In order to find an appropriate working point for later measurements of the HFS spectrum, several combinations of temperature and current of the laser diode are tested. First, the current at the laser is set to $I_{\text{diode}} = (45.1 \pm 0.1)\,\text{mA}$ and four different temperatures in the range between $(29.6 \pm 0.1)\,°\text{C}$ and $(36.1 \pm 0.1)\,°\text{C}$ are applied. The measured signals are shown in Figure 13. For the highest temperature, mode hopping can be observed in the signal.

Furthermore, measurements with the same temperature of $(34.7 \pm 0.1)\,°\text{C}$ but four different currents of the laser diode are performed. The used currents are in the range between $(38.9 \pm 0.1)\,\text{mA}$ and $(57.7 \pm 0.1)\,\text{mA}$. The corresponding plots of the signal are shown in Figure 14. As in the case of the measurements with different temperatures, mode hopping is observed here as well, in the measurement with $I_{\text{diode}} = (51.1 \pm 0.1)\,\text{mA}$. The plot in Figure 14d shows the working point which is used for the measurement of the HFS spectrum. The corresponding signal does not show any signs of mode hopping, making this an appropriate working point.

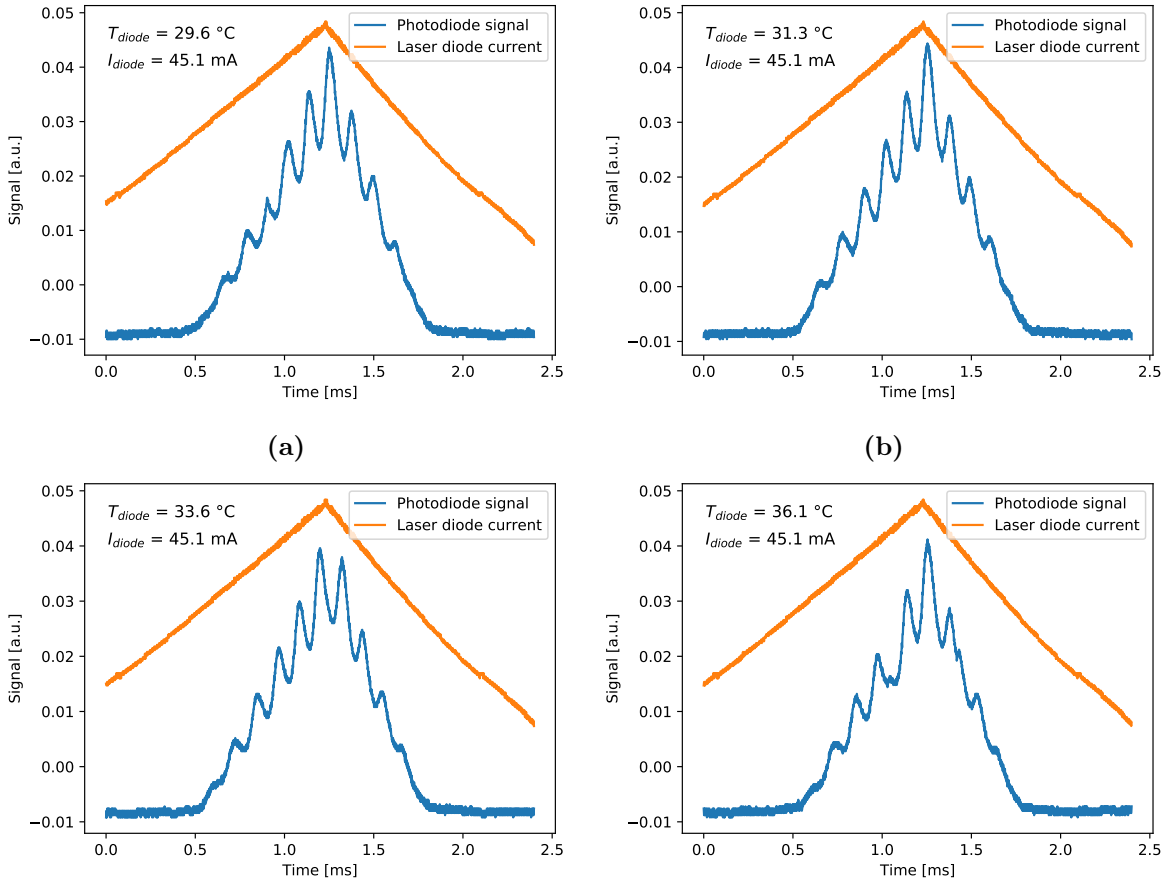

Figure 13: Laser signal with the etalon for different temperatures of the laser diode. The scaling of both signals is chosen such that they are visible together. The current applied to the laser diode is in all four plots $I_{\text{diode}} = (45.1 \pm 0.1)\,\text{mA}$ while four different values for the temperatures are used namely **(a)** $T = (29.6 \pm 0.1)\,°\text{C}$, **(b)** $T = (31.3 \pm 0.1)\,°\text{C}$, **(c)** $T = (33.6 \pm 0.1)\,°\text{C}$ and **(d)** $T = (36.1 \pm 0.1)\,°\text{C}$. Plot **(d)** shows the case where mode hopping occurs at a time right after 1 ms.

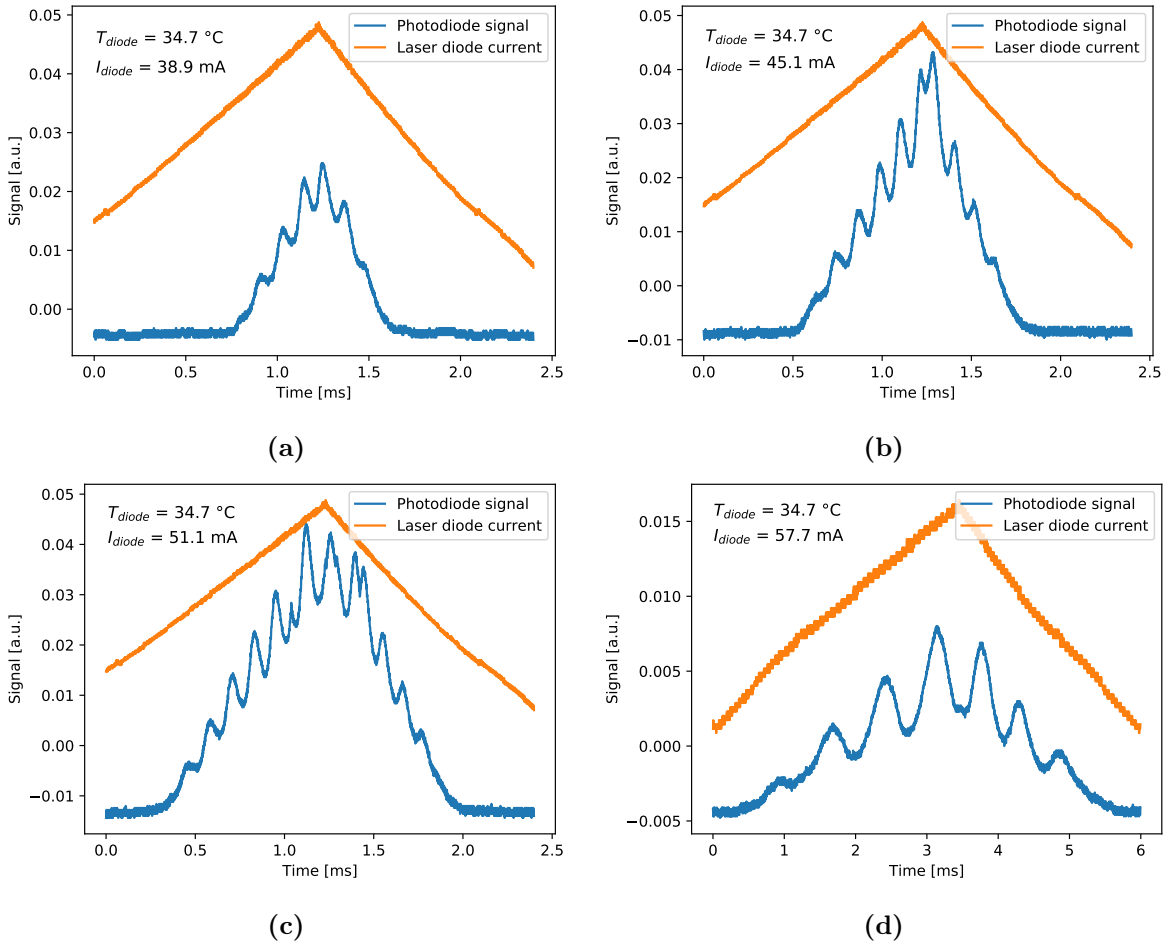

Figure 14: Laser signal with the etalon for different currents of the laser diode. The temperature of the laser diode is in all four plots $T = (34.7 \pm 0.1)\,°\mathrm{C}$ while four different values for the current are used namely **(a)** $I_{\mathrm{diode}} = (38.9 \pm 0.1)\,\mathrm{mA}$, **(b)** $I_{\mathrm{diode}} = (45.1 \pm 0.1)\,\mathrm{mA}$, **(c)** $I_{\mathrm{diode}} = (51.1 \pm 0.1)\,\mathrm{mA}$ and **(d)** $I_{\mathrm{diode}} = (57.7 \pm 0.1)\,\mathrm{mA}$. Plot **(d)** shows the working point used for the measurement of the HFS spectrum later on. As one can see, no mode hoppings occur in when using this working point

4.2 Spectrum of the hyperfine structure

This measurement is performed at a working point of $T = (34.5 \pm 0.1)\,°\mathrm{C}$ Temperature, $I_{\mathrm{diode}} = (57.7 \pm 0.1)\,\mathrm{mA}$ current. The laser current is additionally driven with a triangular shape resulting in $U \approx 1\,\mathrm{V_{pp}}$ voltage of the photodiode, $f \approx 155\,\mathrm{Hz}$ frequency, measured with the oscilloscope. According to subsubsection 3.2.2, a measurement of the HFS-spectrum as well as a measurement to gauge the etalon are performed within the same time range and therefore current range. These measurements are shown in Figure 15.

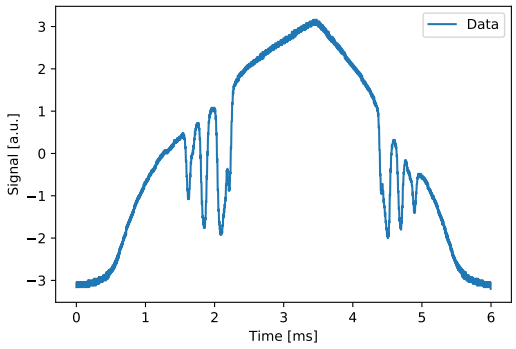

(a) HFS-spectrum at entire measurement range

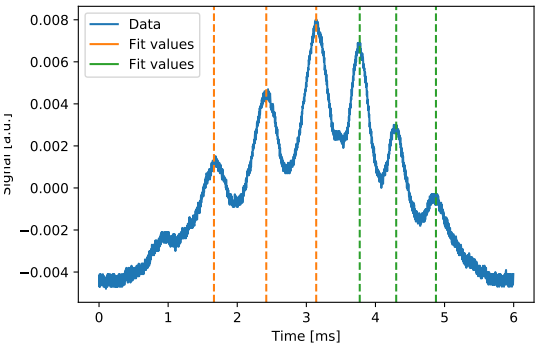

(b) Etalon gauge at entire measurement range

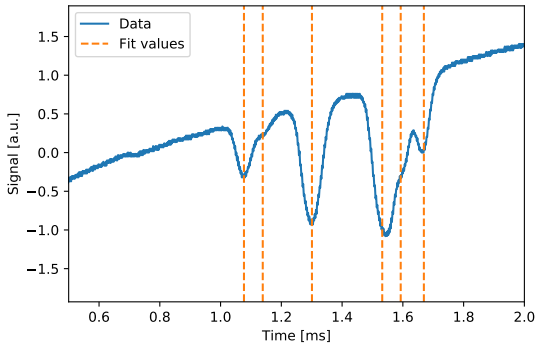

(c) HFS-spectrum left flank in detail

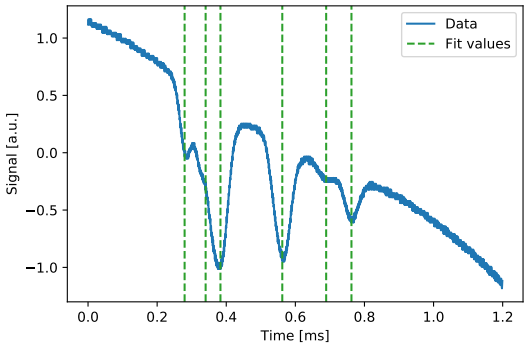

(d) HFS-spectrum right flank in detail

Figure 15: HFS spectrum measurements. The ramping up and ramping down ((**c**) and (**d**)) are evaluated seperately. This also means, that the etalon gauge is also treated seperately for the left and right part. Notice, that the bottom plots do have an arbitrary time offset. But since only time differences are of importance, this does not change the evaluation.

4.2.1 Etalon measurement

First, the etalon measurement, which is shown in Figure 15b, is used to determine the conversion factor between frequency and time $c = \frac{\Delta\nu}{\Delta t}$. This factor is used to calculate the differences in frequency of the measured HFS-lines. The determination of this factor is done separately for both ramp up and ramp down of the current since the slope of the the ramp up and ramp down are not exactly the same. For each etalon peak a fit is performed in order to get the time value of each signal maximum where constructive interference occurs. This is done by adding a gaussian

function with a linear function, resulting in the fit function

$$f_{fit}(t) = N \cdot \exp\left(-\frac{1}{2}\left(\frac{t-t_0}{\sigma}\right)^2\right) + a \cdot t + b, \tag{30}$$

where t_0 represents the center of each gaussian peak. These values of the center are used for the determination of the points of constructive interference. An example plot is shown in Figure 16a. The remaining fits can be seen in Figure 27 in the appendix. All values of the center of the interference maxima are drawn in the plot in Figure 15 and are also listed in Table 2. Afterwards, the differences Δt_0 between the points of constructive interference are calculated. As explained in subsubsection 3.1.2, the difference $\delta\nu$ in frequency corresponding to two neighbouring peaks is known to be $\delta\nu = (9924 \pm 30)\,\mathrm{MHz}$. Since there are three etalon peaks fitted on each side of the ramp, two values for of Δt_0 can be calculated for each side. The weighted average of the respective two values of Δt_0 is calculated to

$$\Delta t_{0_{\text{ramp up}}} = (0.735 \pm 0.003)\,\mathrm{ms} \qquad \Delta t_{0_{\text{ramped down}}} = (0.540 \pm 0.003)\,\mathrm{ms} \tag{31}$$

Thus the conversation factor $c = \frac{\Delta\nu}{\Delta t_0}$ from time to frequency is given by

$$c_{\text{ramped up}} = (-13\,500 \pm 50)\,\mathrm{MHz/ms} \qquad c_{\text{ramped down}} = (18\,400 \pm 100)\,\mathrm{MHz/ms}. \tag{32}$$

The corresponding uncertainties are calculated via gaussian error propagation.

Table 2: Fit values of the etalon peaks. The mean value of a gaussian peak is represented by t_0, the error of this value by s_{t_0}, which are also obtained by the fit. Then the differences Δt_0 are calculated as well as the errors $s_{\Delta t_0}$, which are done via gaussian error propagation.

Ramp	Peak number (chronologically ordered)	t_0 [ms]	s_{t_0} [ms]	Δt_0 [ms]	$s_{\Delta t_0}$ [ms]
up	1	1.663	0.003	-	-
	2	2.420	0.003	0.757	0.004
	3	3.143	0.002	0.723	0.003
down	1	3.772	0.002	-	-
	2	4.300	0.003	0.528	0.004
	3	4.875	0.005	0.575	0.006

4.2.2 HFS spectrum

Now the HFS-spectrum lines from the data in Figure 15c and Figure 15d are determined. The fits are done with the same function as in Equation 30. However, if multiple peaks do overlap, the sum of multiple gaussians is implemented. An example for this is shown in Figure 16b, where two gaussians are fitted at the same time. The plots of the remaining fits can be seen in Figure 28 and Figure 29 in the appendix.

The values of the fit results are shown in Table 3. The different peaks are assigned to the corresponding transitions using the spectral lines shown in Figure 2. The theoretical values of the respective frequency relative to the D1-line are also listed in Table 3. Notice, that the horizontal axis of the plot shown here is inverted compared to the plot in Figure 2, but nevertheless all peaks

in Figure 15c can be assigned unambiguously. The assignment of the peaks to the respective transition is discussed for the ramp up (Figure 15c) in the following.

The double gaussian on the left can be clearly identified as the transitions (^{87}Rb, F:1-2) and (^{87}Rb, F:1-1). The peak in the center of the plot corresponds to the two lines of (^{85}Rb, F:2-3) and (^{85}Rb, F:2-2). Since these two lines are very close to each other, the two corresponding peaks are not distinguishable in the measured spectrum. Therefore, the fit value corresponding to the sum of the two peaks represents a value between the two transition lines. For further calculations, the center of the fitted peak is used for both lines, but the uncertainties of these two lines are set to be the standard deviation of the fitted gaussian. Another possibility would be to fit a double gaussian here to this single peak.

The triple gaussian in the measured spectrum is identified with the transitions (^{85}Rb, F:3-3), (^{85}Rb, F:3-2), (^{87}Rb, F:2-2) and (^{87}Rb, F:2-1). Again, the first intense peak is assigned to two transition lines for the same reasons as before. The complete assignment is also listed in Table 3.

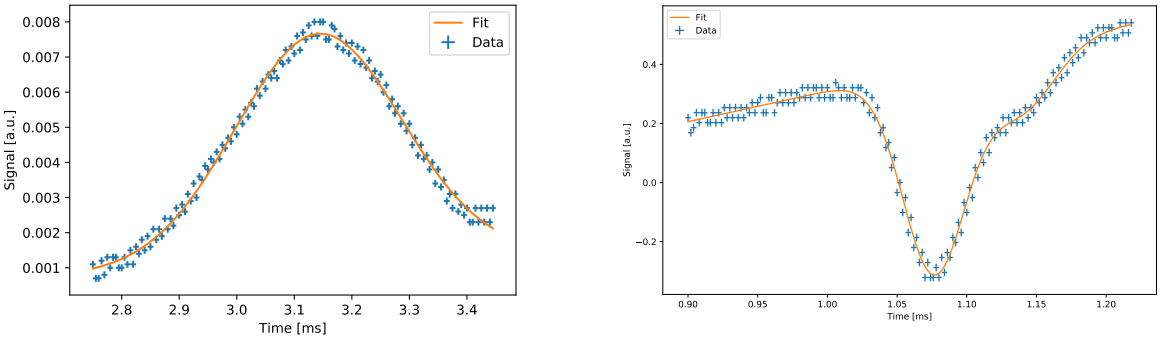

(a) **(b)**

Figure 16: Example fits of the analysis of the etalon measurement and the HFS spectrum analysis. The left side **(a)** shows the fit of the third peak (ramped up) in detail. The right side **(b)**shows the fit of the first and second peak (ramped up) of the HFS spectrum in detail. The errorbars of the data points are given by the resolution of the oscilloscope.

In order to determine the interval constant A given by

$$A = \frac{\Delta E_{HFS}(F+1) - \Delta E_{HFS}(F)}{F+1} = \frac{\nu(F+1)\,h - \nu(F)\,h}{F+1} = \frac{\Delta\nu h}{F+1}\,, \tag{33}$$

the differences in time between the peaks are converted to differences in frequency using the conversion factor c. For ^{87}Rb F is set to 1 in the formula, since the transitions are from $F = 1$ to $F = 2$. Analogously for ^{85}Rb F is set to 2. A sketch of the corresponding energy differences and therefore frequency differences between the possible transitions of the HFS are shown in Figure 11. For the interval constant of each state (^{87}Rb^{2}S$_{1/2}$, ^{87}Rb ^{2}P$_{1/2}$, ^{85}Rb ^{2}S$_{1/2}$, ^{85}Rb ^{2}P$_{1/2}$), there are are in total 4 frequency differences (2 on each side of the ramp) used for the calculation. The uncertainties are calculated via gaussian error propagation. The corresponding results can be found in Table 7 in the appendix. From these values, the weighted averages of the frequency differences are calculated.

The final results for the interval constants according to Equation 33 are listed in Table 4. Since the transitions (^{85}Rb, F:2-3) and (^{85}Rb, F:2-2) as well as (^{85}Rb, F:3-3) and (^{85}Rb, F:3-2) can not be resolved separately in the spectrum, the interval constant of the state ^{85}Rb^{2}P$_{1/2}$ is calculated to 0 MHz.

Table 3: Fit values of the HFS-spectrum peaks. The mean value of a gaussian peak is represented by t_0, the error of this value by s_{t_0}, which are also obtained by the fit. Then the differences Δt_0 are calculated as well as the errors $s_{\Delta t_0}$, which are done via gaussian error propagation. The theoretical values are taken from Figure 2.

Ramp	Peak number (chronologically ordered)	t_0 [ms]	s_{t_0}[ms]	Respective transition	theo. frequency value (relative to D1) [GHz]
up	1	1.077	0.006	^{87}Rb,F:1-2	+4.58
	2	1.139	0.002	^{87}Rb,F:1-1	+3.76
	3	1.3008	0.03	^{85}Rb,F:2-3	+1.92
				^{85}Rb,F:2-2	+1.56
	4	1.532	0.03	^{85}Rb,F:3-3	-1.12
				^{85}Rb,F:3-2	-1.48
	5	1.593	0.006	^{87}Rb,F:2-2	-2.25
	6	1.670	0.001	^{87}Rb,F:2-1	-3.07
down	1	0.2795	0.0003	^{87}Rb,F:2-1	-3.07
	2	0.340	0.003	^{87}Rb,F:2-2	-2.25
	3	0.383	0.02	^{87}Rb,F:2-2	-1.48
				^{85}Rb,F:3-3	-1.12
	4	0.5622	0.02	^{85}Rb,F:2-2	+1.56
				^{85}Rb,F:2-3	+1.92
	5	0.689	0.001	^{87}Rb,F:1-1	+3.76
	6	0.7624	0.0004	^{87}Rb,F:1-2	+4.58

Table 4: Interval constants of the related atomic states.

State	$\Delta\nu$ [MHz]	Interval constant A/h [MHz]
$^{87}Rb^2S_{1/2}$	(7440 ± 20)	3720 ± 10
$^{87}Rb^2P_{1/2}$	(1100 ± 20)	598 ± 8
$^{85}Rb^2S_{1/2}$	(3200 ± 200)	1080 ± 80
$^{85}Rb^2P_{1/2}$	(0 ± 200)	(0 ± 80)

4.3 Double resonance measurement

The double resonance measurement is performed on two different days of the experiment. The main difference between these two measurements is that in the second measurement an attempt is made to rotate the experimental table in order to align it along the horizontal component of the earth's magnetic field.

To obtain the double resonance signal, RF radiation of a frequency of approximately $\nu_{RF} \approx 500\,\text{kHz}$ is used. This frequency is measured with the built-in measuring functions of the oscilloscope and the uncertainty is estimated based on the fluctuations of the value shown on the oscilloscope. The exact values can be found in Table 5 together with the other parameters of the measurements.

The current in coil number 4 is adjusted to maximise the intensity of the double resonance signal. In both measurements the signal is maximal for a current of $I_4 = (90 \pm 1)\,\text{mA}$. Since the signal becomes maximal for complete compensation of the vertical component of the earth's magnetic field, the current of coil number 4 can be used to calculate this component of the stray field. The measured values of the current in coil number 4 are also listed Table 5. The resulting absorption signal and the oscillating magnetic field in horizontal direction are shown for one configuration in Figure 17.

In all measurements the current of coil number 1 is adjusted in order to get equidistant absorption peaks, which means that the offset of the magnetic field generated by coil number 1 is splitting the Zeeman levels such that the energy difference between these levels is equal to the energy carried by the radio frequency photons. Therefore, at the points in time when the oscillating magnetic field is zero, the RF radiation induces transition between the Zeeman levels, leading to a situation where pumping is possible again, i.e. the transparency of the Rb-cell decreases. This leads to equidistant peaks in the absorption signal.

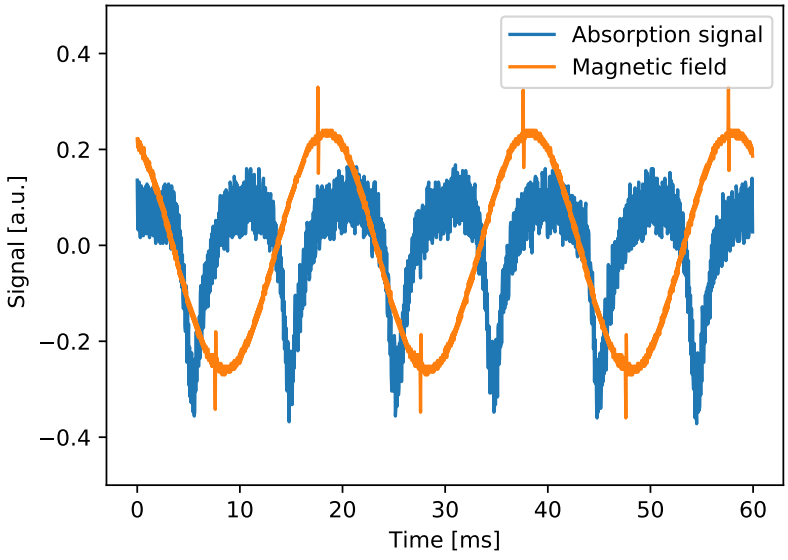

Figure 17: Example plot of the double resonance measurement. The vertical axis is shown in an arbitrary unit since the absorption signal and the signal of the magnetic field are scaled in order to make both signals visible. The parameters used for this measurement are $I_{\text{diode}} = (58.5 \pm 0.1)\,\text{mA}$, $T = 34.6\,^{\circ}\text{C}$, $I_4 = (90 \pm 1)\,\text{mA}$, $\nu_{RF} = (512 \pm 3)\,\text{kHz}$ and $I_1 = (146 \pm 1)\,\text{mA}$.

Table 5: Measured values and used parameters for the double resonance measurement. The two measurements are performed on two different days while the experimental table is aligned along the horizontal component of the earths magnetic field in the second measurement series.

I_{diode} [mA]	T [°C]	I_4 [mA]	ν_{RF} [kHz]	Dir. of current	I_1 [mA]	ΔI_1 [mA]
58.5 ± 0.1	34.6	90 ± 1	512 ± 3	normal	146 ± 1	11.0 ± 1.4
				reversed	135 ± 1	
59.0 ± 0.1				normal	100 ± 1	13.0 ± 1.4
				reversed	87 ± 1	
58.8 ± 0.1	34.5	88 ± 1	510 ± 3	normal	148 ± 1	20.0 ± 1.4
				reversed	128 ± 1	
59.3 ± 0.1				normal	102 ± 1	19.0 ± 1.4
				reversed	83 ± 1	

4.3.1 Calculation of the vertical component of the earth's magnetic field

Using the conversion factor $k_4 = (4.76 \pm 0.01) \cdot 10^{-4} \, \frac{\text{T}}{\text{A}}$ between current and magnetic field given in section 3, Table 1, the vertical component of the stray field is then

$$B_{\text{earth}}^{\text{vert}} = I_4 \cdot k_4 \tag{34}$$

and the corresponding uncertainty is calculated via gaussian error propagation as

$$s_{B_{\text{earth, vert}}} = B_{\text{earth}}^{\text{vert}} \cdot \sqrt{\left(\frac{s_{I_4}}{I_4}\right)^2 + \left(\frac{s_{k_4}}{k_4}\right)^2} \, . \tag{35}$$

The resulting values for the two different measurement series are

$$B_{\text{earth, 1}}^{\text{vert}} = (42.8 \pm 0.5) \, \mu\text{T} \quad \text{and} \quad B_{\text{earth, 2}}^{\text{vert}} = (41.9 \pm 0.5) \, \mu\text{T} \, , \tag{36}$$

Calculating the weighted average of these two values using the exact numbers yields

$$B_{\text{earth, 1}}^{\text{vert}} = (42.4 \pm 0.3) \, \mu\text{T} \, . \tag{37}$$

4.3.2 Calculation of the horizontal component of the earth's magnetic field

As explained before, the magnetic field in horizontal direction created by coil number 1 is adjusted in order to create a Zeeman splitting corresponding to the incident radio frequency radiation. However, since the effective horizontal magnetic field B_{eff} in the Rb cell is the sum of the horizontal component of the earth's magnetic field $B_{\text{earth}}^{\text{hor}}$ and the field $B_{\text{coil 1}}$ created by coil number 1,

$$B_{\text{eff}} = B_{\text{earth}}^{\text{hor}} + B_{\text{coil 1}} \, , \tag{38}$$

the magnetic field corresponding to the incident radio frequency is not exactly $B_{\text{coil 1}}$. Instead, it is either smaller than $B_{\text{coil 1}}$, in case the earth's magnetic field is anti parallel to the field of coil number 1 or larger than $B_{\text{coil 1}}$ in case the earth's magnetic field is parallel to the field generated by

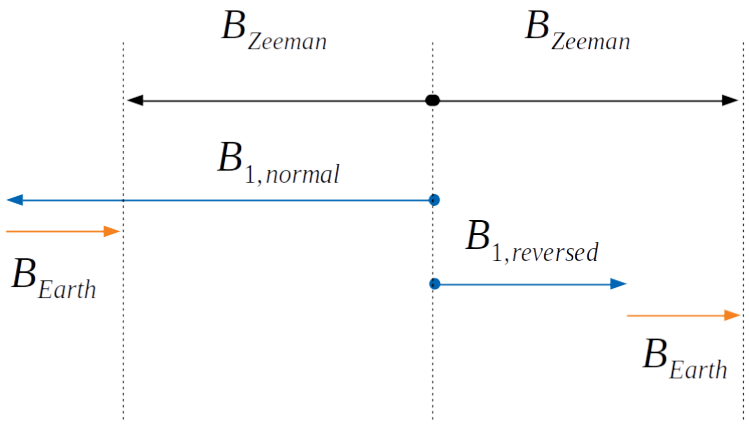

Figure 18: Alignment of the horizontal magnetic fields. B_{Zeeman} shows the field which is necessary to have to get a transition with the radio frequency of $\approx 500\,\mathrm{KHz}$. If the polarity of the current is normal ($B_{1,\text{ normal}}$) the earth magnetic field is anti parallel to the field of coil 1 and therefore the current needs to be higher. If its parallel ($B_{1,\text{ reversed}}$), the fields add up together and a lower current is needed.

coil number 1. A sketch of the two different cases is shown in Figure 18. Using this, the horizontal component of the earth's magnetic field can be determined by performing each measurement with both parallel and anti parallel setting alignment of $B_{\text{coil 1}}$ and $B^{\text{hor}}_{\text{earth}}$. This is realised by changing the direction of the current of coil 1 between the measurements. The two different directions of the current are referred to as *normal* polarisation and *reversed* polarisation.

For both directions of the current in coil number 1, the current is adjusted such that B_{eff} is equal to the magnetic field B_{Zeeman} needed to create a Zeeman splitting corresponding to the incident radio frequency radiation

$$B_{\text{eff}} = B_{\text{Zeeman}}\,. \tag{39}$$

Therefore, the difference between the two values of the current in coil 1 is two times the current needed to compensate the horizontal component of the stray field

$$\Delta I_1 = I_{1,\text{ normal}} - I_{1,\text{ reversed}} = \frac{B_{1,\text{ normal}} - B_{1,\text{ reversed}}}{k_1} \tag{40}$$

$$= \frac{B_{\text{Zeeman}} + B^{\text{hor}}_{\text{earth}} - \left(B_{\text{Zeeman}} - B^{\text{hor}}_{\text{earth}}\right)}{k_1} \tag{41}$$

$$= 2\,\frac{B^{\text{hor}}_{\text{earth}}}{k_1}\,, \tag{42}$$

with $I_{1,\text{ normal}}$ and $I_{1,\text{ reversed}}$ being the current applied at coil number 1 for the normal polarity and the reversed polarity and $k_1 = (7.99 \pm 0.01) \cdot 10^{-4}\,\mathrm{T/A}$ being the conversion factor given in section 3, Table 1. Using this relation, the horizontal component of the earths magnetic field and

the corresponding uncertainty are calculated to

$$B_{\text{earth}}^{\text{hor}} = \frac{\Delta I_1 \cdot k_1}{2} \quad \text{and} \quad s_{B_{\text{earth}}^{\text{hor}}} = \frac{B_{\text{earth}}^{\text{hor}}}{2} \cdot \sqrt{\left(\frac{s_{\Delta I_1}}{\Delta I_1}\right)^2 + \left(\frac{s_{k_1}}{k_1}\right)^2}\,. \tag{43}$$

The resulting values of the two measurement series are

$$B_{\text{earth, 1}}^{\text{hor}} = (4.4 \pm 0.3)\,\mu\text{T} \quad \text{and} \quad B_{\text{earth, 2}}^{\text{hor}} = (5.2 \pm 0.3)\,\mu\text{T} \tag{44}$$

for the measurements without aligning the experimental tables along the earths magnetic field and

$$B_{\text{earth, 3}}^{\text{hor}} = (8.0 \pm 0.3)\,\mu\text{T} \quad \text{and} \quad B_{\text{earth, 4}}^{\text{hor}} = (7.6 \pm 0.3)\,\mu\text{T} \tag{45}$$

for the measurements with aligning the experimental table properly. The mean values of the two results for both measurement series are

$$B_{\text{earth, not aligned}}^{\text{hor}} = (4.8 \pm 0.2)\,\mu\text{T} \quad \text{and} \quad B_{\text{earth, aligned}}^{\text{hor}} = (7.8 \pm 0.2)\,\mu\text{T}\,. \tag{46}$$

Since the current needed to compensate the horizontal component of the stray field is significantly larger for the measurement with the aligned table, this effect seems to be quite relevant. Furthermore, combining the results of the two measurement series is not reasonable since they represent different magnetic fields as the first measurement only accounts for a smaller part of the horizontal component of the earths magnetic field since the table is not aligned along the earths magnetic field.

4.3.3 Calculation of the nuclear spin of the two Rubidium isotopes

The nuclear spin of the two isotopes is calculated using the effective constant magnetic field in the Rb-cell, which is

$$B_{\text{eff}} = I_{\text{eff}} \cdot k_1 = \frac{I_{1,\text{ normal}} + I_{1,\text{ reversed}}}{2} \cdot k_1\,. \tag{47}$$

Using Equation 10, the nuclear spin of the two isotopes is then given by

$$I_{\text{nuclear spin}} = \frac{\mu_B \cdot B_{\text{eff}}}{h \cdot \nu_{RF}} - \frac{1}{2}\,, \tag{48}$$

and the corresponding uncertainty is calculated with gaussian error propagation to

$$s_{I_{\text{nuclear spin}}} = \frac{\mu_B}{h} \cdot \sqrt{\left(\frac{k_1}{\nu_{RF}} s_{I_{\text{eff}}}\right)^2 + \left(\frac{I_{\text{eff}}}{\nu_{RF}} s_{k_1}\right)^2 + \left(\frac{k_1\, I_{\text{eff}}}{\nu_{RF}^2} s_{\nu_{RF}}\right)^2}\,. \tag{49}$$

The resulting values of the first measurement series are

$$I_{^{85}\text{Rb},1} = 2.569 \pm 0.018 \quad \text{and} \quad I_{^{87}\text{Rb},1} = 1.542 \pm 0.012 \tag{50}$$

and the second measurement yields

$$I_{^{85}\text{Rb},2} = 2.526 \pm 0.018 \quad \text{and} \quad I_{^{87}\text{Rb},2} = 1.528 \pm 0.012\,. \tag{51}$$

With these results, the working point of the lower current in the laser diode can be assigned to the isotope ^{85}Rb and the higher current to the isotope ^{87}Rb using the literature values

$$I^{\text{lit}}_{^{85}\text{Rb}} = 2.5 \quad \text{and} \quad I^{\text{lit}}_{^{87}\text{Rb}} = 1.5\,. \tag{52}$$

As for the results for the horizontal component of the magnetic field, an average of the results of the two different measurement series is not reasonable since the horizontal magnetic field measured in the two runs is a quantity included in the calculations of the nuclear spin, but changed between the runs due to changes of the experimental setup. Therefore, the two measurements should not be combined.

4.4 Spin precession

In order to observe the spin precession of the atoms in a magnetic field, only the vertical component of the earth's magnetic field is used. Therefore, the horizontal component of the earth's magnetic field is compensated using a current of $I_1 = (10 \pm 1)\,\text{mA}$, which is the value determined in the double resonance measurement. As in the previous part of the experiment, the rotated position of the experimental table is used for this part as well in order to compensate the horizontal component of the stray field completely. The working point of $I_{\text{diode}} = (58.8 \pm 0.1)\,\text{mA}$ and $T = (34.5 \pm 0.1)\,°\text{C}$ is used for this measurement, since the signal is found to be stronger compared to the signal at the higher working point. A rectangular current from zero to a certain value is applied to coil number 5. Thus, the magnetic field from this source is basically getting switched on and off. When the magnetic field is turned off, the spin precession can be seen.

4.4.1 Calculation of the vertical component of the earth's magnetic field

The measured signal of the spin precession is shown in Figure 19a. This signal is triggered with the rectangular pulse applied to coil number 5. Using equation Equation 8, the vertical component of the earth's magnetic field can be calculated from the period T_L of the spin precession. The period is calculated by identifying the time interval of a full period for each oscillation in the measured signal. Afterwards, the mean of the values T_{L_i} is taken as T_L.

The corresponding plot is shown in Figure 19b with the dashed green lines being the points t_i in time which are estimated to show full periods. These points are determined by eye. The uncertainty of these estimations is set to $s_{t_i} = 0.2\,\mu\text{s}$. Since the value of each of the periods T_{L_i} is the difference between two neighbours of these points, the uncertainty for each value of the period is $s_{T_{L_i}} = s_{t_i}/\sqrt{2}$.

The mean value for the period is then calculated to

$$T_L = (5.01 \pm 0.05)\,\mu\text{s}\,, \tag{53}$$

where the uncertainty is given by $s_{T_L} = s_{T_{L_i}}/\sqrt{N}$, with N being the number of values included in the mean. By rearranging Equation 8 and using $\omega_L = 2\pi\,/\,T_L$, the vertical component of the earth's magnetic field and the corresponding uncertainty can then be calculated with

$$B^{\text{vert}}_{\text{earth}} = \frac{h}{g_F\,\mu_B\,T_L} \quad \text{and} \quad s_{B^{\text{vert}}_{\text{earth}}} = B^{\text{vert}}_{\text{earth}} \cdot \frac{s_{T_L}}{T_L}\,. \tag{54}$$

Inserting the value of the period stated above yields

$$B^{\text{vert}}_{\text{earth, 2}} = (42.8 \pm 0.5)\,\mu\text{T}\,, \tag{55}$$

with $g_F = \frac{1}{3}$, corresponding to the pumped state ^{85}Rb $^2\text{S}_{1/2}$, [3, p.14].

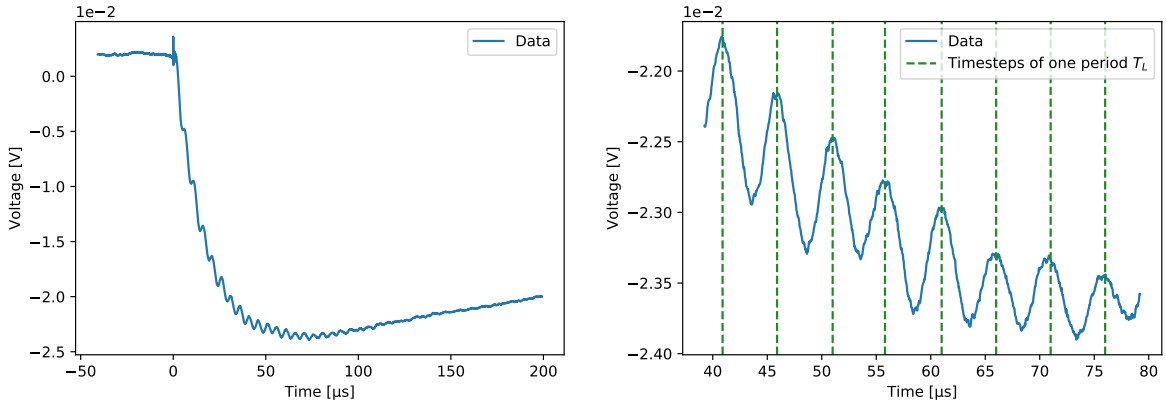

(a) **(b)**

Figure 19: Measured data of the spin precession. The horizontal component of the earth's magnetic field is compensated while the vertical component is the magnetic field which is responsible for the precession. Plot **(a)** shows the measured data while and **(b)** shows a zoomed in plot of the same data including the time steps used for the calculation of the precession period.

4.4.2 Spin precession after partially compensating the stray field

In order to see the behaviour of the spin precession when changing the strength of the vertical magnetic field, coil number 4 is used to partially compensate the vertical component of the magnetic field. The resulting signal for a current of $I_4 = (51 \pm 1)\,\mathrm{mA}$ is shown in Figure 20. As expected from the theoretical relation in Equation 8, the period of the precession increases when the magnetic field is smaller. The same calculations as explained in the previous subsection are performed for this setting, resulting in

$$T_{\text{part.comp.}} = (11.34 \pm 0.16)\,\mu\mathrm{s} \quad \text{and} \quad B_{\text{part.comp.}} = (18.9 \pm 0.3)\,\mu\mathrm{T}\,. \tag{56}$$

This result is consistent with the previously calculated vertical component of the earths magnetic field, considering that the sum of $B_{\text{part.comp.}}$ and the magnetic field of coil number 4, which is in this case $B_4 = k_4 \cdot I_4 = 24.3\,\mu\mathrm{T}$, have to add up to the same value as $B^{\text{vert}}_{\text{earth, 2}}$ in Equation 55.

As shown in Figure 21, the spin precession vanishes almost entirely when the earths magnetic field is compensated completely. In this case, a current of $I_4 = (90 \pm 1)\,\mathrm{mA}$ is applied to coil number 4.

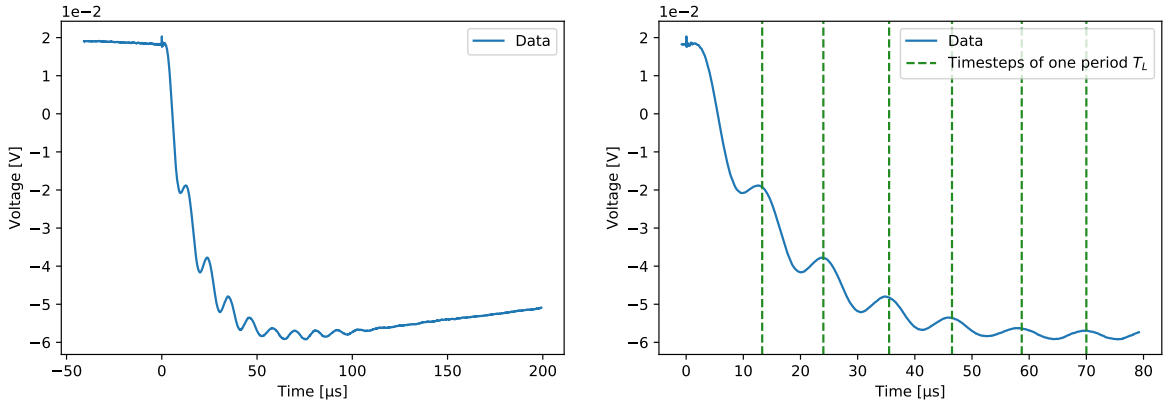

(a) **(b)**

Figure 20: Measured data of the spin precession after partially compensating the stray field. Plot **(a)** shows the measured data while and **(b)** shows a zoomed in plot of the same data including the time steps used for the calculation of the precession period.

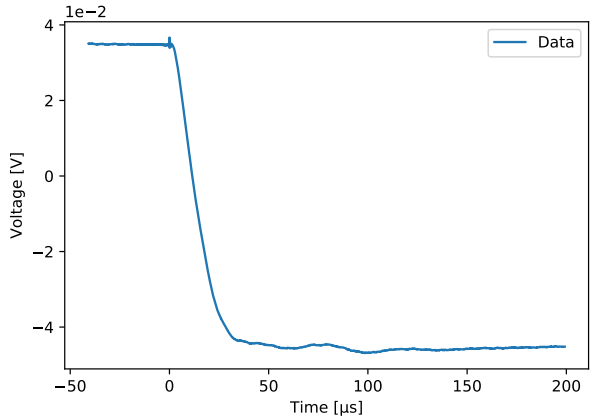

Figure 21: Measured data of the spin precession signal with full compensation of the stray field. As a result of the compensation of the magnetic field, no spin precession can be observed.

4.5 Measurement of the relaxation time

The relaxation time of the system is determined with the two different methods explained in subsubsection 3.2.5 and subsubsection 3.2.6.

4.5.1 Dehmelt method

For both isotopes the relaxation time of the system is determined using the Dehmelt method. The current on the laser diode is $I_{\text{diode}} = (58.8 \pm 0.1)\,\text{mA}$ for the isotope ^{85}Rb and $I_{\text{diode}} = (59.3 \pm 0.1)\,\text{mA}$ for the isotope ^{87}Rb. During both measurement series, the measured temperature of the laser diode is $T = 34.6\,°\text{C}$. In order to compensate the earths magnetic field, the current of the coil number one and number four are set to $I_1 = (10 \pm 1)\,\text{mA}$ and $I_4 = (90 \pm 1)\,\text{mA}$. For both working points 6 different neutral filters are used to reduce the intensity of the laser light. An alternating step function is applied to coil number 3 in order to create an alternating constant magnetic field in the horizontal direction. The used filters are listed in Table 6. For each intensity the increasing curve of the transmitting laser light after the reversal of the magnetic field is fitted to the function

$$f(t) = a \cdot e^{-t \cdot b} + c\,. \tag{57}$$

The parameter $b = 1/\tau$ in this fit function is the inverse of the orientation time, which is related to the relaxation time as shown in Equation 25.

Two example plots for the determination of the orientation time are shown in Figure 22 for the working point of the isotope ^{85}Rb without any filter and with the filter of optical density $D = 1.0$. The relative intensity which is calculated using Equation 23 and the resulting fit parameters are listed in Table 6. The plots of the other fits can be seen in Figure 32 and Figure 33 in the appendix.

Table 6: Used filters and resulting fit parameters in the measurement of the relaxation time using the Dehmelt method. The fit parameter $b = 1/\tau$ is shown for both measurement series, i.e. for both isotopes.

Filtername	Transmittance	$1\,/\,\tau$ $[\text{s}^{-1}]$	
		^{85}Rb	^{87}Rb
-	1.000	1366 ± 11	2010 ± 6
D 0.3	0.501	625 ± 2	1043 ± 3
D 0.6	0.251	534 ± 1	872 ± 6
D 1.0	0.100	327 ± 1	617 ± 7
D 1.3	0.050	276 ± 2	540 ± 14
D 2.0	0.010	186 ± 6	454 ± 12
D 2.3	0.005	240 ± 13	488 ± 15

The values of the inverted orientation time are plotted as a function of the relative intensity x in Figure 23a for the isotope ^{85}Rb and in Figure 23b for the isotope ^{87}Rb. A linear fit with the function

$$g(x) = m + d \cdot x \tag{58}$$

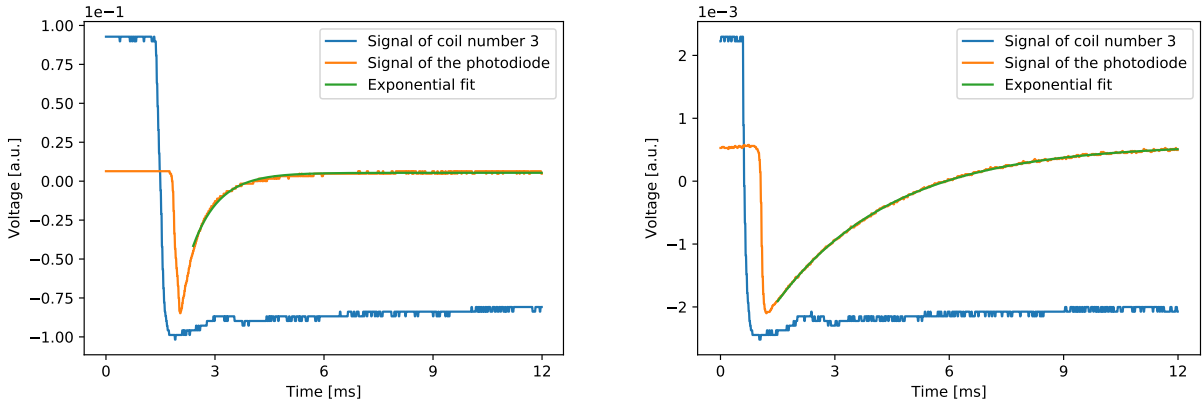

(a) **(b)**

Figure 22: Measured data and the corresponding exponential fit for the Dehmelt method. Both measurements are performed at a workingpoint corresponding to ^{85}Rb using **(a)** no neutral filter and **(b)** the filter with optical density $D = 1.0$. In both measurements the averaging function of the oscilloscope is used. In both plots the signal of coil number 3 is scaled in order to make both signals visible in the same plot.

is performed for both isotopes, leading to the fit parameters

$$m_{^{85}\mathrm{Rb}} = (250 \pm 30)\,\mathrm{s}^{-1} \quad \text{and} \quad d_{^{85}\mathrm{Rb}} = (910 \pm 140)\,\mathrm{s}^{-1} \tag{59}$$

for ^{85}Rb and to

$$m_{^{87}\mathrm{Rb}} = (400 \pm 80)\,\mathrm{s}^{-1} \quad \text{and} \quad d_{^{87}\mathrm{Rb}} = (1480 \pm 150)\,\mathrm{s}^{-1} \tag{60}$$

for the isotope ^{87}Rb. According to the method explained in subsubsection 3.2.5, the offset m of this fit is equal to the inverse of the relaxation time T_R. The resulting uncertainty s_{T_R} of the relaxation time is calculated from the uncertainty s_m of the y-axis offset with gaussian error propagation as

$$s_{T_R} = \sqrt{\left(\frac{\partial T_R}{\partial m}\, s_m\right)^2} = \sqrt{\left(\frac{-1}{m^2}\, s_m\right)^2} = \frac{s_m}{m^2}\,. \tag{61}$$

This results in the relaxation time

$$T_{R,\mathrm{Dehmelt},\,1} = (4.1 \pm 0.5)\,\mathrm{ms} \quad \text{and} \quad T_{R,\mathrm{Dehmelt},\,2} = (2.5 \pm 0.5)\,\mathrm{ms}\,. \tag{62}$$

The weighted average of these two values yields

$$T_{R,\mathrm{Dehmelt}} = (3.3 \pm 0.3)\,\mathrm{ms}\,, \tag{63}$$

whereby the unrounded values are used for this calculation.

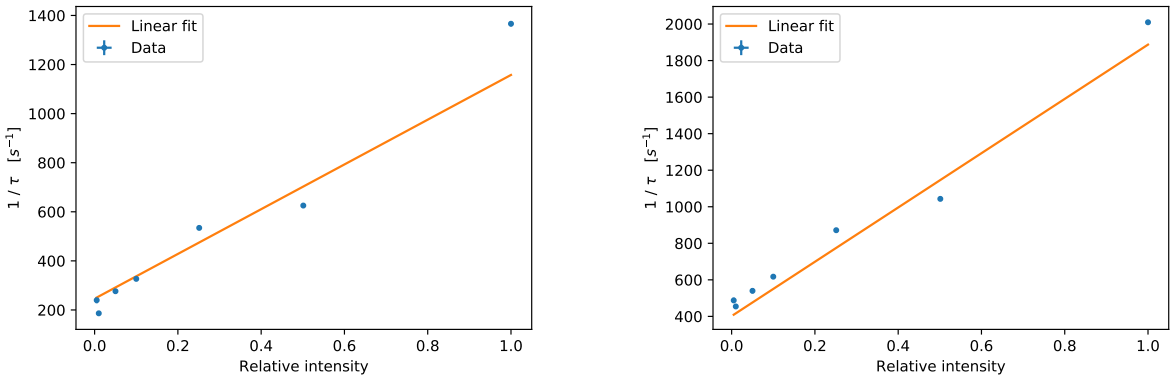

(a) **(b)**

Figure 23: Linear fit for the determination of the relaxation time using the Dehmelt method. At **(a)** the working point corresponding to ^{85}Rb and **(b)** the working point corresponding to ^{87}Rb. The errors of the data points are drawn in the graph, although they are too small to be visible.

4.5.2 Franzen method

This measurement is performed at the lower working point at $I_{\text{diode}} = 58.8\,\text{mA}$, with a temperature of $T = 34.6\,°\text{C}$ and DC settings on both photodiode and oscilloscope. The data of the different chopper velocities are evaluated like shown in Figure 24. In this section I_{trans} is the intensity of the transmitted light, which is measured with the photodiode and oscilloscope. Since the oscilloscope only shows voltage values corresponding to the intensity, all following plots are set to have arbitrary units (a.u.) on this axis.

First, the values of the start and end points of the relaxation, i.e. the time Δt during which the laser is blocked, are calculated.

As these start and end points are corresponding to either a steep ascent or descent of the intensity, this is done by calculating the gradient at all data points and checking if the value of the gradient is either above a certain threshold (corresponding to the end point of the relaxation) or below a certain threshold (steep descent, corresponding to the starting point of the relaxation).

E.g. at a starting point, the difference of two values (i.e. the gradient) is starting to get very low. If they differ by a certain threshold (1.5 units of raw data from the oscilloscope), this point is considered to be a start point.

Furthermore, the evaluation point of $I_{trans}(\Delta t)$ is shifted by 0.1 ms from the end point. This is done due to the fact that an end point corresponds to one of the last data points before the signal of the laser is back. Since the signal is expected to jump to a certain value and then increase again as shown in Figure 12, the steep increase at the beginning is not considered to be part of the exponential increase of the transmission signal due to pumping.

The time after which the transmission signal is back is estimated to be approximately 0.1 ms. Thus, Δt is defined as the time difference of the evaluation point with the starting point. Now Δt is calculated by the average of the differences of the evaluation- and starting points. $I_{trans}(\Delta t)$ is then given by the average of the I_{trans} values of the evaluation points.

This procedure is performed for 10 different data samples, each corresponding to a different chopper time. Furthermore, the special case $\Delta t = 0$ is considered by evaluating the transmission intensity at the starting point of the relaxation. The plots of all choppertimes can be seen in Figure 34 and Figure 35. The error of Δt is set to be two time steps of the oscilloscope, which varies for each data set because of different time scopes of the oscilloscope. The uncertainty of

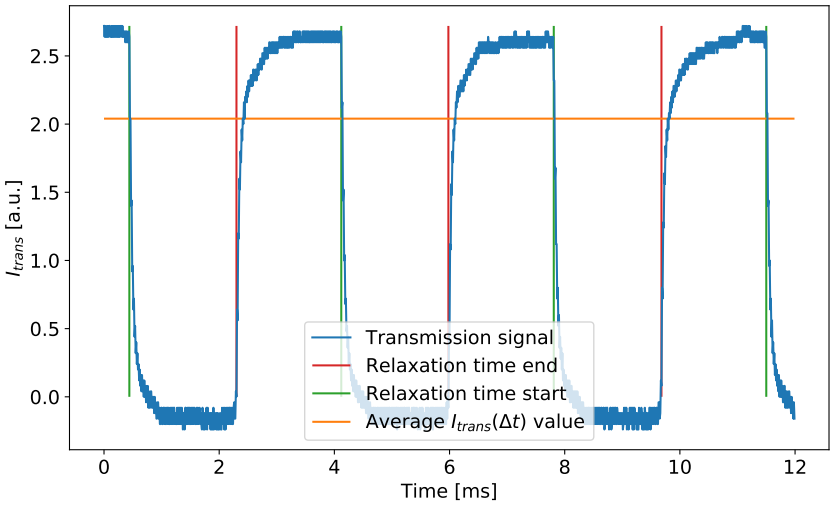

Figure 24: Evaluation with Franzen method. The intensity of the transmitted light is plotted against the time. The relaxation time Δt is measured by the average of the differences of the evaluation point ("relaxation time end" (red) shifted by 0.1 ms) with the "relaxation time start" (green). The $I_{trans}(\Delta t)$ value is then given by the value at the evaluation point. The orange horizontal line shows the average of the $I_{trans}(\Delta t)$ values.

the intensity comes from taking the difference between the intensity two time steps ahead with the intensity at the evaluation point and the same with two time steps before.

Based on this, the relaxation times Δt are plotted against transition signals $I_{trans}(\Delta t)$ and fitted with an exponential of the form

$$I_0 \cdot \exp \frac{-t}{T_{R_{\text{Franzen}}}} + z \,, \tag{64}$$

where I_0 is the maximum intensity, t the time, $T_{R_{\text{Franzen}}}$ the relaxation time and z an offset caused by the way the oscilloscope works. Due to the scale of the oscilloscope, the intensity is negative during the dark times. However, this is not a problem as shifting the data on this axis does not change the physics. The fit is shown in Figure 25. Since the error bars are quite big at the bottom, there is a second plot with cutted error bars to make the exponential more visible. This plot can be found in Figure 35 in the appendix. The fit results in the relaxation time

$$T_{R,\text{Franzen}} = (2.7 \pm 1.7)\,\text{ms}\,. \tag{65}$$

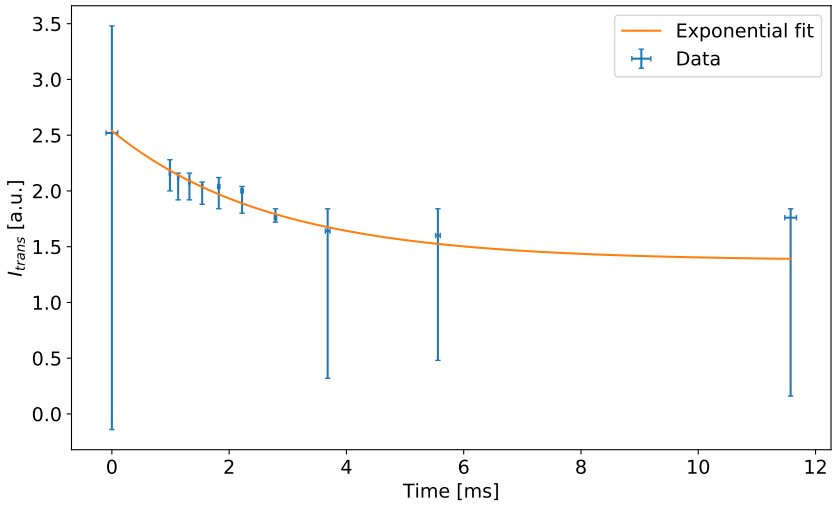

Figure 25: Exponential fit of the intensity at different relaxation times. To make the exponential more visible, there is also a plot with a cutted frame, which can be found in the appendix at Figure 36.

5 Summary and discussion

In the first part of the experiment, the spectrum of the hyperfine structure of the two isotopes ^{85}Rb and ^{87}Rb is measured. The different peaks of the spectrum are successfully fitted with gaussian peaks and subsequently assigned to the corresponding transitions of the HFS spectrum. This allows to calculate the interval constants A of the two isotopes. The resulting values are listed in the table below together with the corresponding literature values, which are taken from reference [5].

State	Interval constant A/h [MHz]	Literature value A_{lit}/h [MHz]
$^{87}\text{Rb}^2\text{S}_{1/2}$	3720 ± 10	3417.3
$^{87}\text{Rb}^2\text{P}_{1/2}$	598 ± 8	409.1
$^{85}\text{Rb}^2\text{S}_{1/2}$	1080 ± 80	1011.9
$^{85}\text{Rb}^2\text{P}_{1/2}$	0 ± 80	120.7

The measured values for the isotope ^{87}Rb can not confirm the literature value within the statistical uncertainties. However, these uncertainties are very small due to the small uncertainties of the fit parameters used for the calculation.

The interval constants calculated for the isotope ^{85}Rb can confirm the literature value within one standard deviation for the $^2\text{S}_{1/2}$ state and within two standard deviations for the $^2\text{P}_{1/2}$ state. It should be noted again, that the calculated value for the $^2\text{S}_{1/2}$ state of ^{85}Rb is zero since the different lines needed for the calculation of this value could not be resolved. However, due to the uncertainty of 80 MHz, this value can still confirm the literature value within it's statistical uncertainty. This could probably be improved by fitting the sum of two gaussians to the third and fourth peak (current ramped up), where only a single gaussian is fitted in this analysis. Although this might be difficult to do, this could lead into the separation of the two lines and giving a more reasonable result than 0 MHz.

The double resonance measurement is used in order to determine both the vertical and the horizontal component of the earths magnetic field as well as the nuclear spin of the two Rubidium isotopes. For this part of the experiment two different runs are performed, where the experimental table is rotated in the second run. This is done in order to align the coils which lie in horizontal direction with the horizontal component of the earth magnetic field. The vertical component of the earth's magnetic field is calculated in both runs. Since the rotation of the experimental table in the horizontal plane does not change the vertical component of the earth's magnetic field, the results of the two runs are combined. The mean of these two values yields

$$B^{\text{vert}}_{\text{earth, 1}} = (42.4 \pm 0.3)\,\mu\text{T}\,. \tag{66}$$

This value agrees within two standard deviations with the literature value $B^{vert}_{\text{earth, lit}} = 42.9\,\mu\text{T}$ [5, p.14].

The resulting values for the horizontal component of the earth's magnetic field are

$$B^{\text{hor}}_{\text{earth, not aligned}} = (4.8 \pm 0.2)\,\mu\text{T} \quad \text{and} \quad B^{\text{hor}}_{\text{earth, aligned}} = (7.8 \pm 0.2)\,\mu\text{T}\,. \tag{67}$$

The resulting values of $B^{\text{hor}}_{\text{earth}}$ obtained in the two different runs differ by approximately 63 %. This discrepancy and the fact that the resulting value of the second run is the larger one indicate that the result of the first run does only correspond to part of the horizontal component of the earths magnetic field. However, even the result of the second run is significantly smaller than the literature value $B^{\text{hor}}_{\text{earth, lit}} = 20.9\,\mu\text{T}$ [5, p.14] and thus can not confirm the literature value. A possible explanation of this difference could be the presence of another external magnetic field in the horizontal direction, which is not considered in the experiment.

The results for the measurement of the nuclear spin are summarised in the following table.

Run	Isotope	Measured nuclear spin	Literature value [5, p.14]
1	^{85}Rb	2.569 ± 0.018	2.5
	^{87}Rb	1.542 ± 0.012	1.5
2	^{85}Rb	2.526 ± 0.018	2.5
	^{87}Rb	1.528 ± 0.012	1.5

The results of the first run of the double resonance measurement only agree with the literature values within 4 standard deviations. However, the relative difference of the literature values and the measured values is only 2.7 % for both isotopes. The deviations between the results of the second run and the literature values are much smaller. Here, the literature values lie within two standard deviations from the measured value for ^{85}Rb and within three standard deviations from the measured values for ^{87}Rb. The relative difference is in this case 1.0 % for ^{85}Rb and 1.9 % for ^{87}Rb. The literature values of the nuclear spin of both isotopes can therefore be confirmed.

The signal of the spin precession in earth's magnetic field can be observed for different strengths of the magnetic field. Furthermore, as expected, the spin precession vanishes when the earth's magnetic field is entirely compensated. The vertical component of the magnetic field is measured to

$$B^{\text{vert}}_{\text{earth, 2}} = (42.8 \pm 0.5)\,\mu\text{T}\,. \tag{68}$$

This value agrees within one standard deviation with the literature value $B^{vert}_{\text{earth, lit}} = 42.9\,\mu\text{T}$ [5, p.14]. The good agreement of the of the two results $B^{\text{vert}}_{\text{earth, 1}}$ and $B^{\text{vert}}_{\text{earth, 2}}$ indicates that there

are no further stray fields in this direction, since the two results are determined with different methods, reducing the possibility of effects leading to systematic errors.

The relaxation time T_R of the Rb-cell is determined using the Dehmelt method. The transmission signals can be fitted very well. This means that the data confirms the theoretical behaviour of an exponential increase to the maximum signal I_0. Thus the uncertainties the fits are leading to are very small. The time constants are plotted against the relative intensities, which are calculated from the optical densities label on each of them. These, however, can also have uncertainties, which is not taken into account. These values are drawn into in a plot in which a linear fit is made. Due to the very small errorbars, the fit does not lie within the uncertainty of most of the data points. This could be explained by the fact the uncertainties may be too small. In general though, the linear tendency is visible for both isotopes. Extrapolating the linear fit to an intensity of zero yields the relaxation time. Doing this for both isotopes and calculating the weighted average of these two values yields

$$T_{R,\text{Dehmelt}} = (3.3 \pm 0.3)\,\text{ms}\,. \tag{69}$$

Obtaining the start and end points can be done precisely since the signal has a clear edge at these points in time. However, it is rather difficult to determine the intensity after the dark time, because at the end point there is no laser light shining in and no signal can be detected. Therefore some time has to pass until the signal is getting back. The determination of this time can not be made unambiguously. In this experiment it is set to 0.1 ms. The error of the intensity gets very large, especially in the lower direction, because varying the time around the evaluation point has a big effect of the intensity since it is exponentially rising. Therefore, is this delay between the end of the dark time and the evaluation point for the current is estimated wrong, this leads to a quite large systematic error. This systematic error would mean that all the measured intensities are then either too small or too large, depending on if the delay is set too short or too long.

The exponential decrease of the relaxation curve is then reconstructed by plotting the intensity values against the dark times. The fit curve lies within all errorbars. This results in a relaxation time of

$$T_{R,\text{Franzen}} = (2.7 \pm 1.7)\,\text{ms}\,. \tag{70}$$

The values of both Dehmelt and Franzen method confirm each other. The value of the Dehmelt method is considered more reliable since the error caused by the uncertainty of the intensity values in the Franzen method has a great impact. This is reflected in the fact that the errors of the relaxation time determined by the Dehmelt method is much smaller than the one obtained by the Franzen method.

Both values do not agree neither with the value of 5.7 ms from [3, p.83], nor with the theoretical value of the longitudinal relaxation time of 5.9 ms, but they are in the same order of magnitude. However, both literature values might not be comparable with the measured values, because the relaxation time depends on different parameters such as pressure, temperature and dimensions of the cell body. It is impossible to make sure these parameters are the same as in the measurement performed in [3, p.83] which led to the literature value of 5.7 ms. Furthermore, the theoretical longitudinal relaxation time calculated with Equation 18 might also differ from the measured values since this formula only considers relaxation processes caused by collisions with the glass cell and does not take collisions with the buffer gas into account.

Another consideration could be that the relaxation times may vary for the both isotopes. In subsubsection 3.2.5 the relaxation time is measured for both isotopes separately but than averaged. This might not be appropriate since the isotopes may interacting differently causing the relaxation processes to have different impacts. Also the distribution of the isotopes may have an effect on this. To investigate this further, the Franzen method could also be executed for the ^{87}Rb. If

this would result in a major difference to ^{85}Rb this could be a hint, different interaction and the distribution are effects of greater impact and the relaxation time has to be declared separately.

6 References

[1] Alfred Kastler. *Nobel Lecture: Optical Methods for Studying Hertzian Resonances*. Nobel Media AB 2020, 1966. URL: https://www.nobelprize.org/uploads/2018/06/kastler-lecture.pdf.

[2] Hans Kopfermann. *Über optisches Pumpen an Gasen*. 1960.

[3] Clemens Baur. "Einrichtung des Versuches "Optisches Pumpen mit Laserdioden"". University of Freiburg, 1997.

[4] ETH Zürich. *Physik IV - Einführung in die Quantenmechanik*. URL: https://qudev.phys.ethz.ch/static/content/science/BuchPhysikIV/PhysikIVch15.html.

[5] M.Koehli. *Versuchsanleitung optisches Pumpen*. 2011.

[6] ILX Lightwave Corporation. *An Overview of Laser Diode Characteristics*. 2005. URL: https://www.newport.com/medias/sys_master/images/images/he9/hd7/8797049520158/AN05-Laser-Diode-Characteristics-Overview.pdf.

7 Appendix

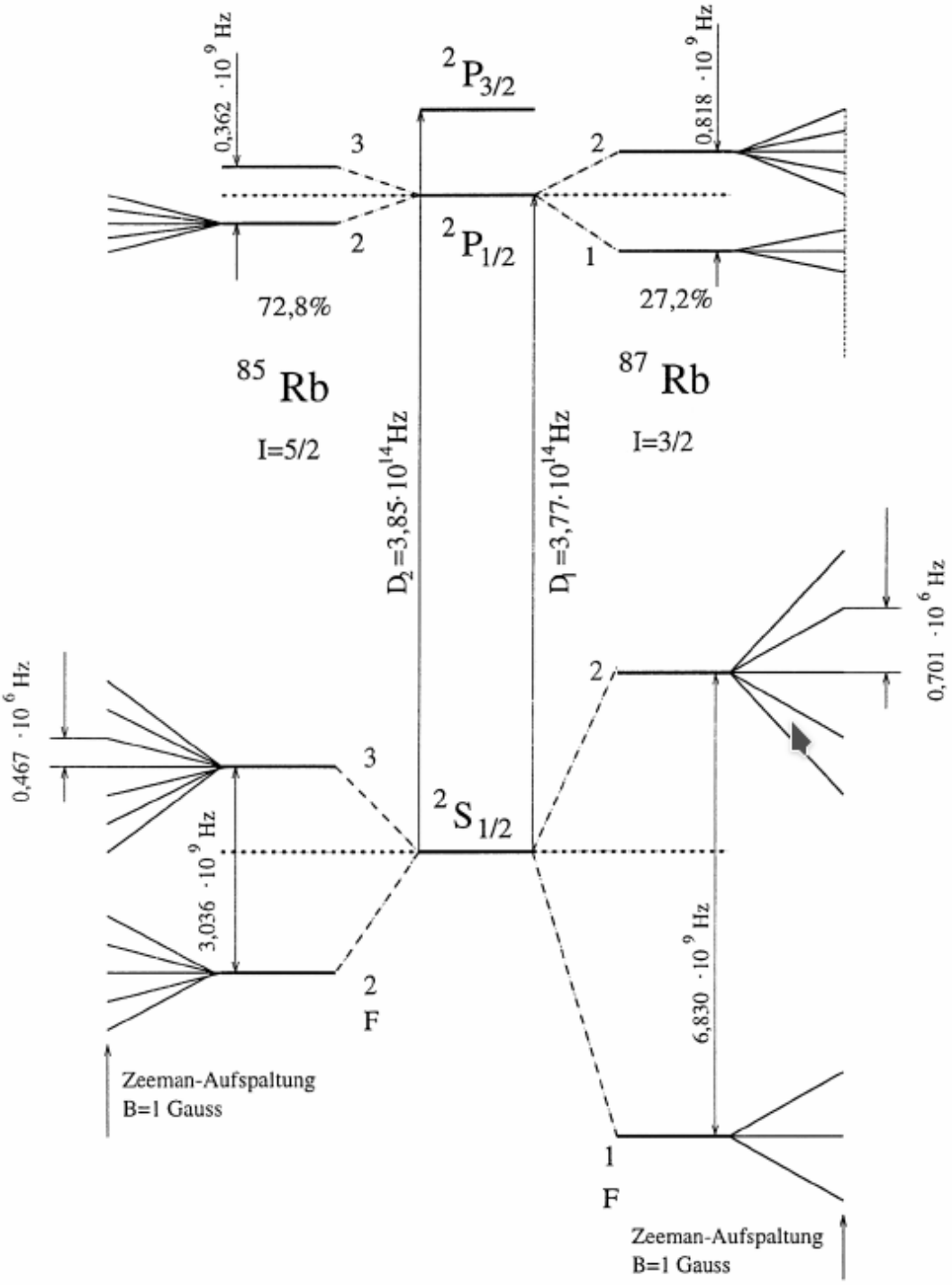

Figure 26: Termsceme for ^{85}Rb and ^{87}Rb [3, p.15]. The energy scaling is not appropriate.

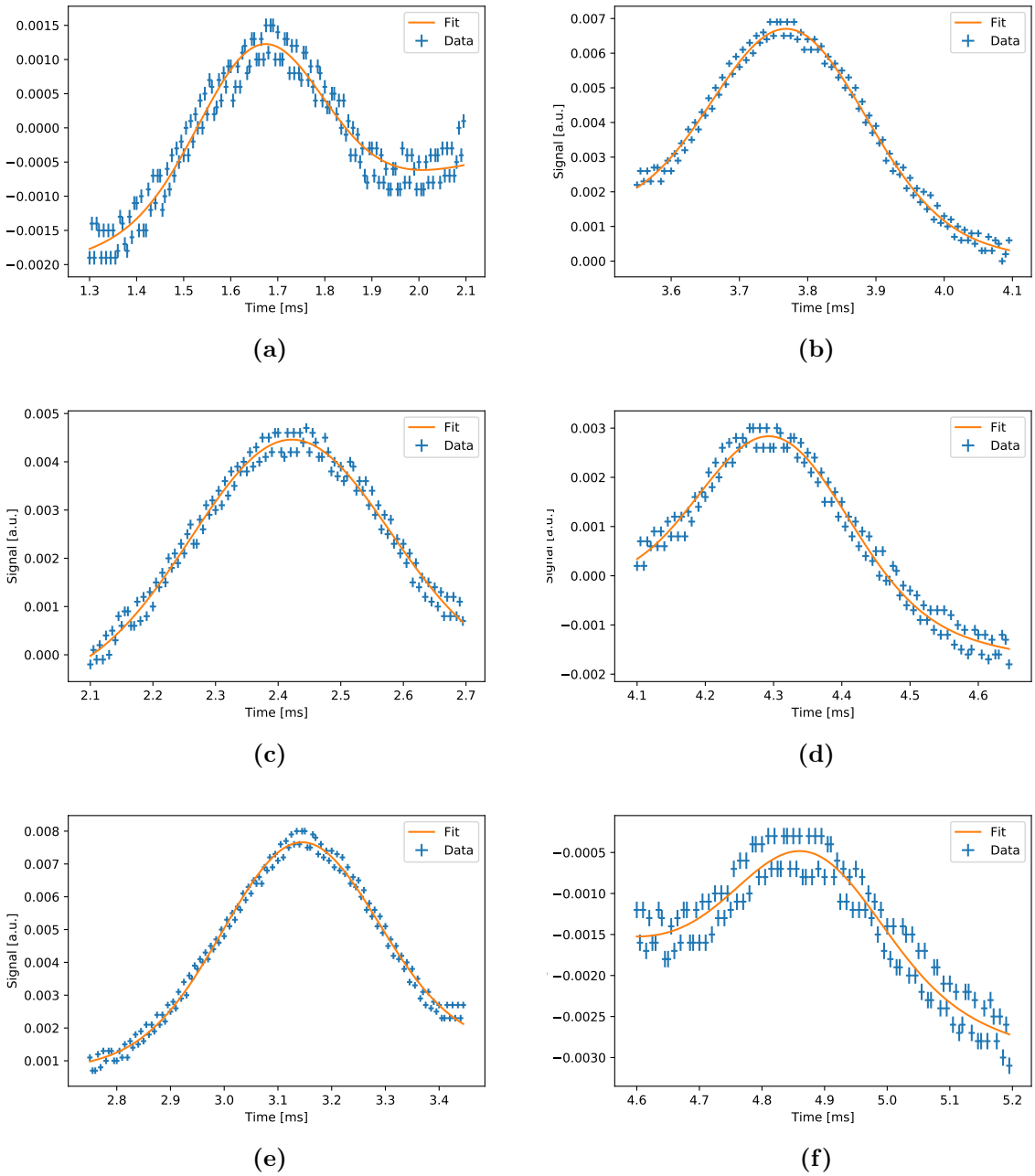

Figure 27: Fits of the etalon measurement (see Figure 15b). On the left side, there are the left flank peak, on the right side, there are the right flank peaks.

Table 7: Differences in frequency for difference of two transitions with $\Delta F = 1$. The time differences Δt are calculated with the values in Table 3, as well as the errors $s_{\Delta t}$.

Ramp	Corresponding state	Considered transitions	Δt [ms]
up	$^{87}Rb^2S_{1/2}$	^{87}Rb,F:1-1 - ^{87}Rb,F:2-1	(0.530 ± 0.002)
		^{87}Rb,F:1-2 - ^{87}Rb,F:2-2	(0.516 ± 0.006)
	$^{87}Rb^2P_{1/2}$	^{87}Rb,F:2-2 - ^{87}Rb,F:2-1	(0.076 ± 0.006)
		^{87}Rb,F:1-2 - ^{87}Rb,F:1-1	(0.062 ± 0.002)
	$^{85}Rb^2S_{1/2}$	^{85}Rb,F:2-2 - ^{85}Rb,F:3-2	(0.23 ± 0.04)
		^{85}Rb,F:2-3 - ^{85}Rb,F:3-3	(0.023 ± 0.004)
	$^{85}Rb^2S_{1/2}$	^{85}Rb,F:3-3 - ^{85}Rb,F:2-3	(0.00 ± 0.04)
		^{85}Rb,F:2-3 - ^{85}Rb,F:2-2	(0.00 ± 0.04)
down	$^{87}Rb^2S_{1/2}$	^{87}Rb,F:1-1 - ^{87}Rb,F:2-1	(0.422 ± 0.004)
		^{87}Rb,F:1-2 - ^{87}Rb,F:2-2	(0.410 ± 0.001)
	$^{87}Rb^2P_{1/2}$	^{87}Rb,F:2-2 - ^{87}Rb,F:2-1	(0.073 ± 0.001)
		^{87}Rb,F:1-2 - ^{87}Rb,F:1-1	(0.061 ± 0.004)
	$^{85}Rb^2S_{1/2}$	^{85}Rb,F:2-2 - ^{85}Rb,F:3-2	(0.18 ± 0.03)
		^{85}Rb,F:2-3 - ^{85}Rb,F:3-3	(0.18 ± 0.03)
	$^{85}Rb^2S_{1/2}$	^{85}Rb,F:3-3 - ^{85}Rb,F:2-3	0.00 ± 0.03
		^{85}Rb,F:2-3 - ^{85}Rb,F:2-2	(0.00 ± 0.03)

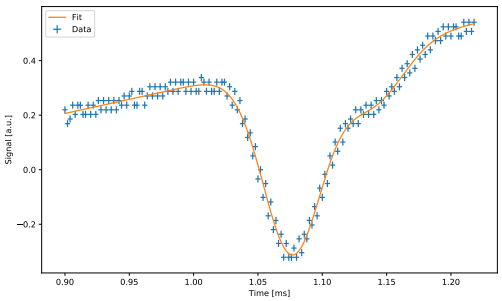

(a) Left peak 1 and 2

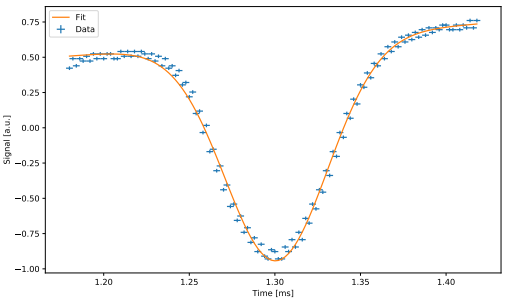

(b) Left peak 3

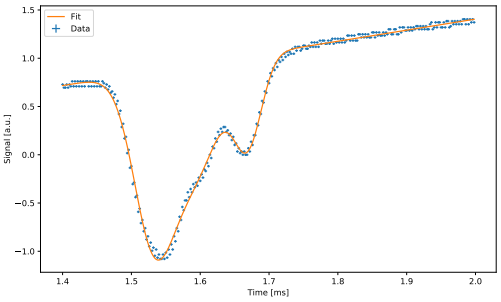

(c) Left peak 4, 5 and 6

Figure 28: Fits of the HFS-spectrum measurement of the left flank (see Figure 28). Ordered chronologically.

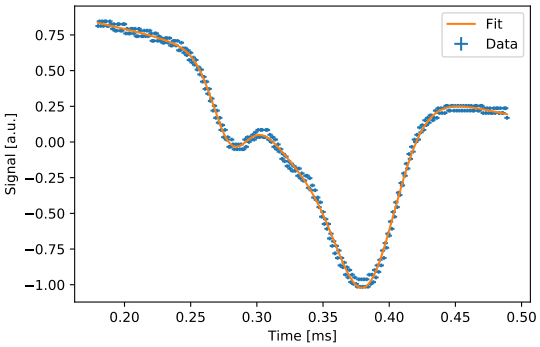

(a) Right peak 1, 2 and 3

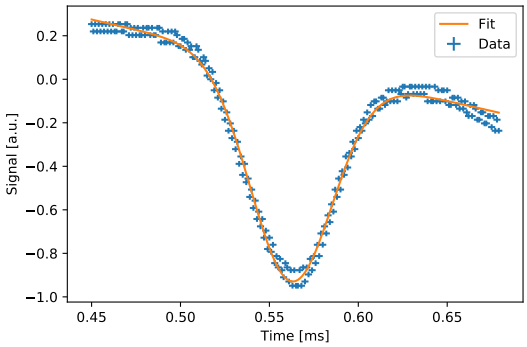

(b) Right peak 4

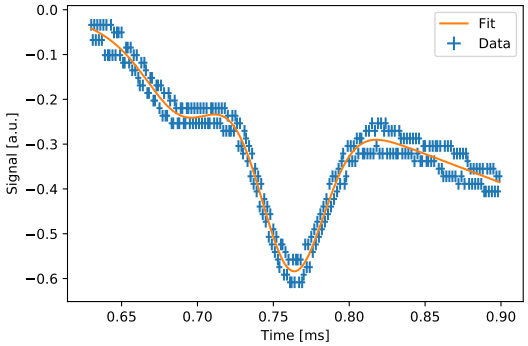

(c) Right peak 5 and 6

Figure 29: Fits of the HFS-spectrum measurement of the right flank (see Figure 29). Ordered chronologically.

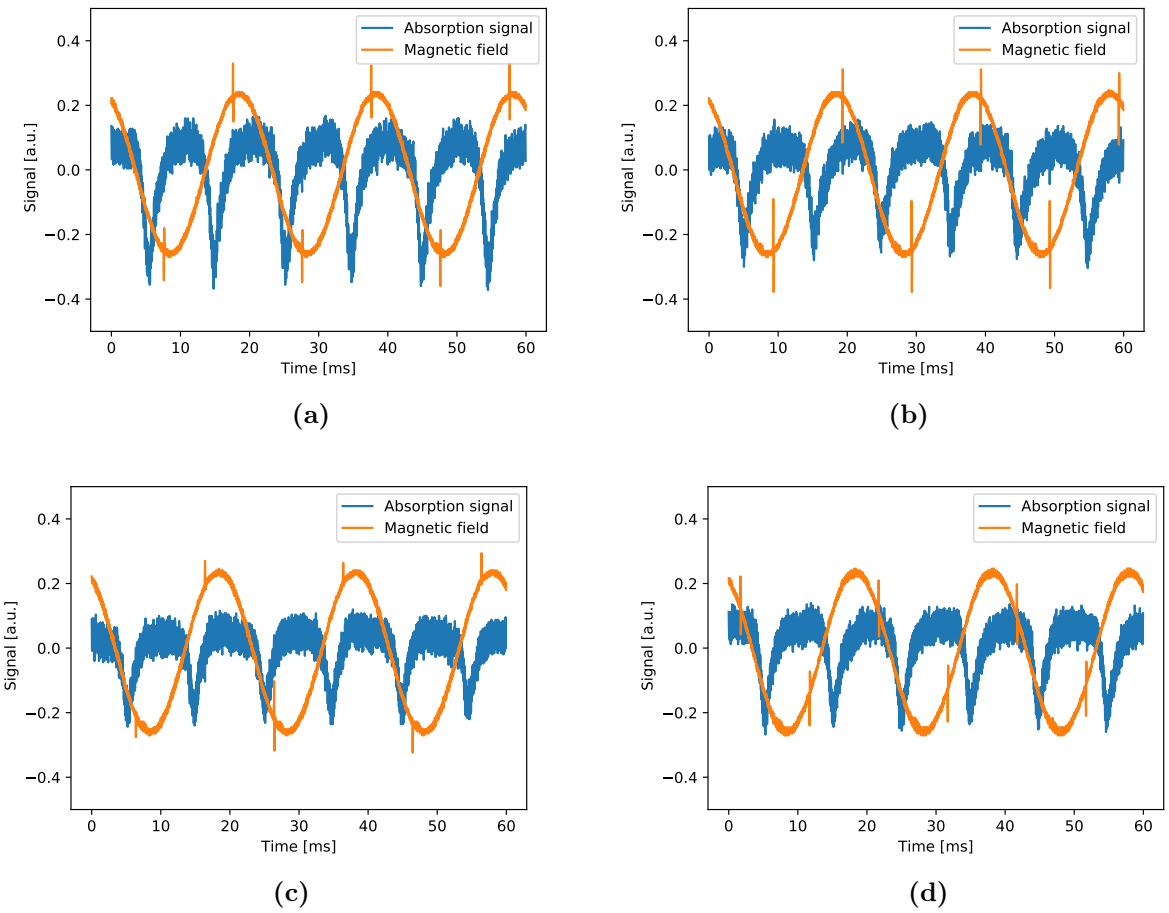

Figure 30: Data measured in the first measurement series of the double resonance measurement. The upper plots correspond to the working point with $I_{\text{diode}} = (58.5 \pm 0.1)\,\text{mA}$ with **(a)** "normal" polarity of the current in coil 1 and **(b)** "reversed" polarity. The lower plots correspond to the working point with $I_{\text{diode}} = (59.0 \pm 0.1)\,\text{mA}$ with **(c)** "normal" polarity of the current in coil 1 and **(d)** "reversed" polarity.

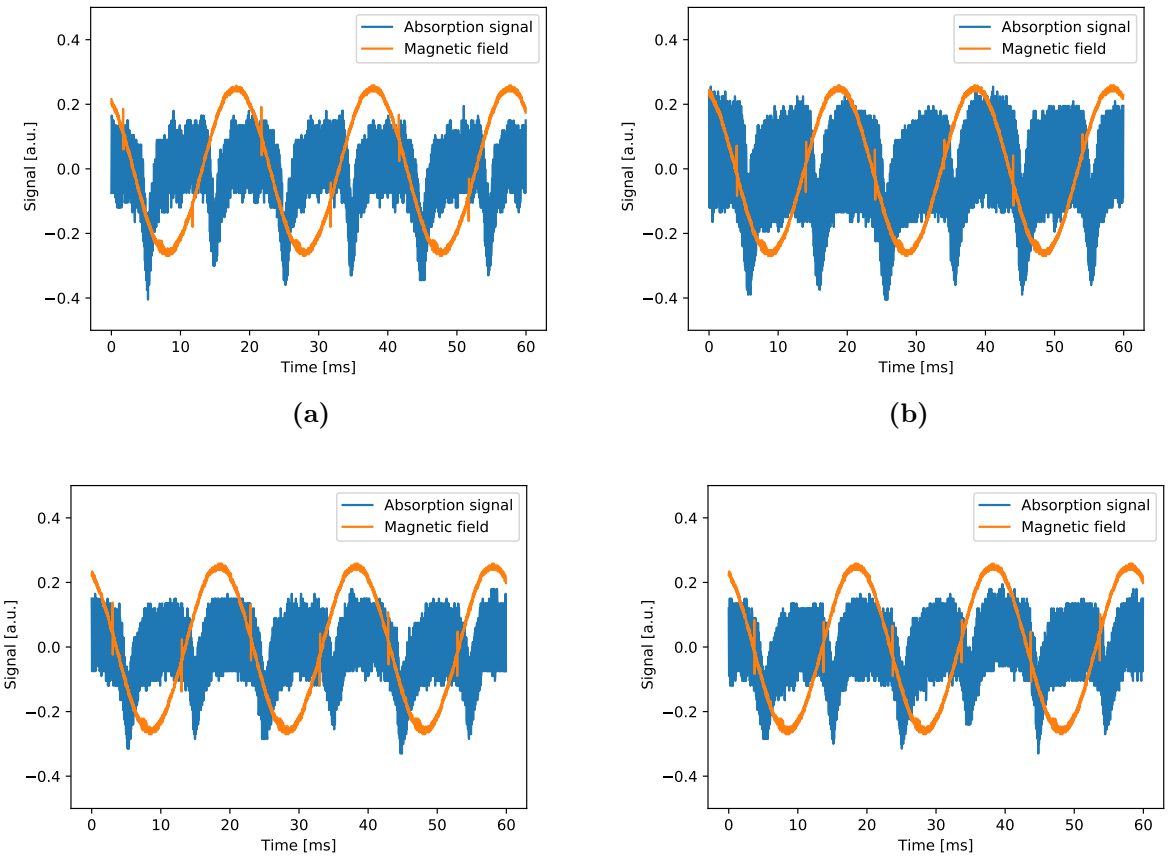

Figure 31: Data measured in the second measurement series of the double resonance measurement after aligning the experimental table along the horizontal component of the earth's magnetic field. The upper plots correspond to the working point with $I_{\text{diode}} = (58.8 \pm 0.1)\,\text{mA}$ with **(a)** "normal" polarity of the current in coil 1 and **(b)** "reversed" polarity. The lower plots correspond to the working point with $I_{\text{diode}} = (59.3 \pm 0.1)\,\text{mA}$ with **(c)** "normal" polarity of the current in coil 1 and **(d)** "reversed" polarity.

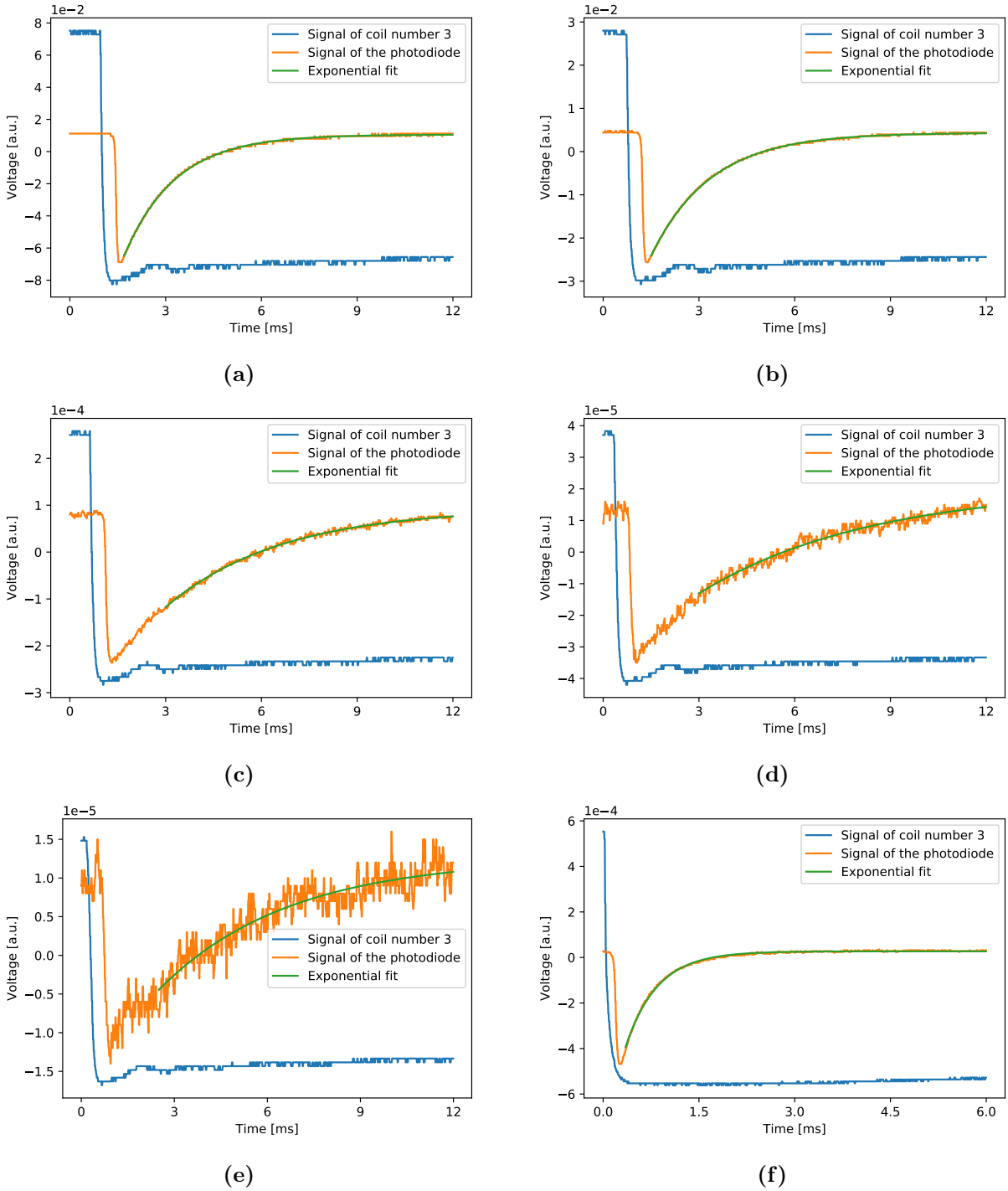

Figure 32: Measured data and the corresponding exponential fit for the Dehmelt method. Measurements **(a)** - **(e)** are performed at the working point corresponding to ^{85}Rb using the filter with optical density **(a)** $D = 0.3$, **(b)** $D = 0.6$, **(c)** $D = 1.3$, **(d)** $D = 2.0$ and **(e)** $D = 2.3$. The measurement corresponding to figure **(f)** is performed at the working point corresponding to ^{85}Rb without using a neutral filter. In all plots the signal of coil number 3 is scaled in order to make both signals visible in the same plot.

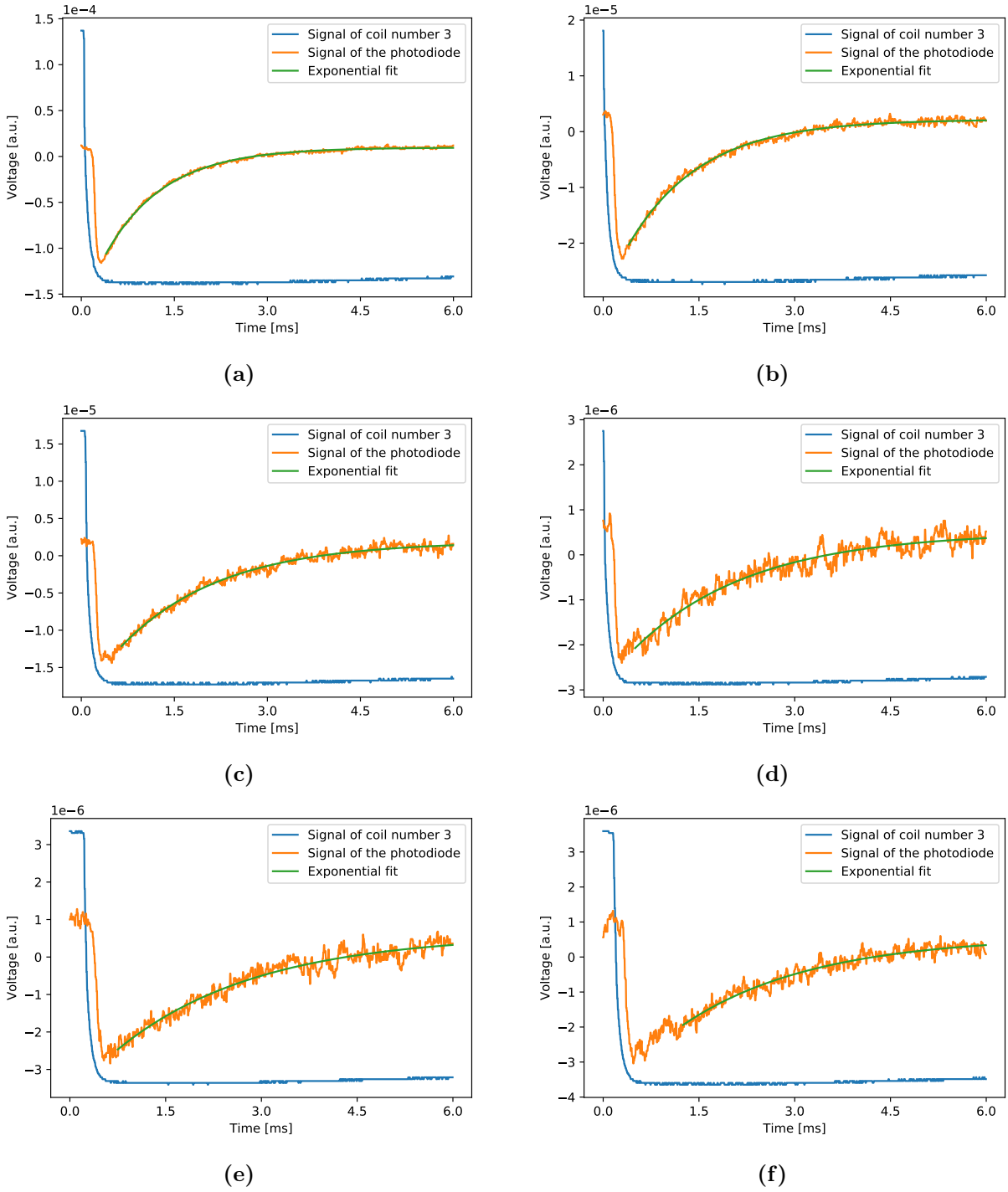

Figure 33: Measured data and the corresponding exponential fit for the Dehmelt method. All measurements are performed at the working point corresponding to ^{87}Rb using the filter with optical density **(a)** $D = 0.3$, **(b)** $D = 0.6$, **(c)** $D = 1.0$, **(d)** $D = 1.3$, **(e)** $D = 2.0$ and **(f)** $D = 2.3$. In all plots the signal of coil number 3 is scaled in order to make both signals visible in the same plot.

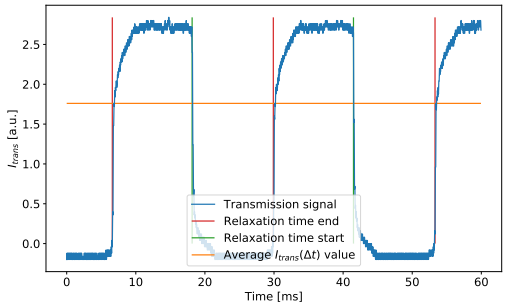

(a) Chopper velocity 1

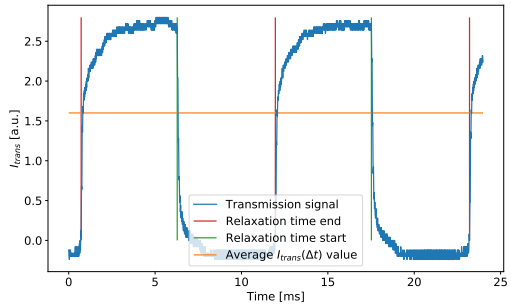

(b) Chopper velocity 2

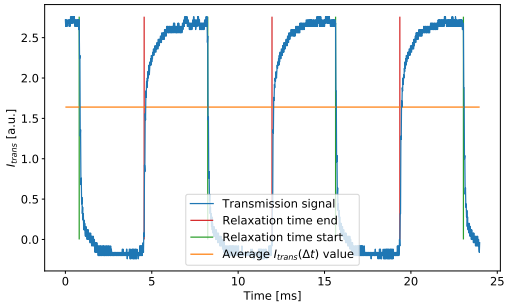

(c) Chopper velocity 3

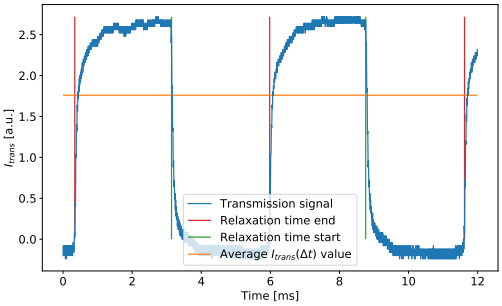

(d) Chopper velocity 4

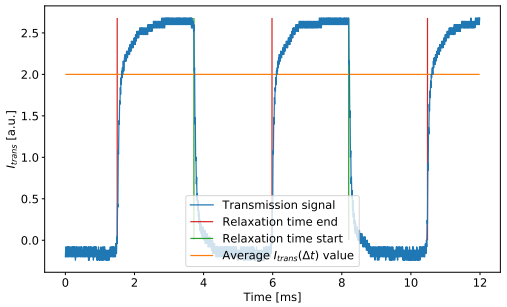

(e) Chopper velocity 5

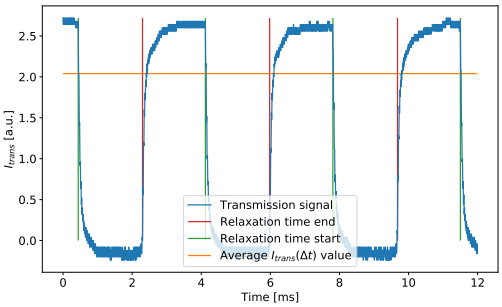

(f) Chopper velocity 6

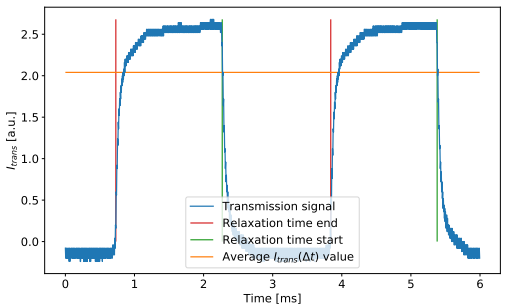

(g) Chopper velocity 7

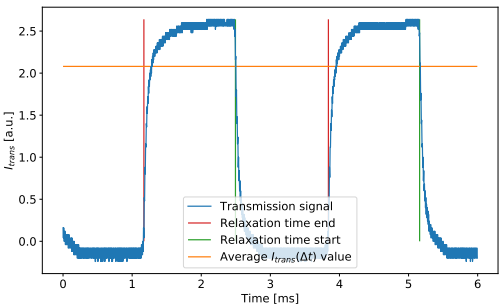

(h) Chopper velocity 8

Figure 34: Transition signal at all chopper velocities, data part one (as explained in subsubsection 3.2.6). Example description of the plots can be seen in Figure 24.

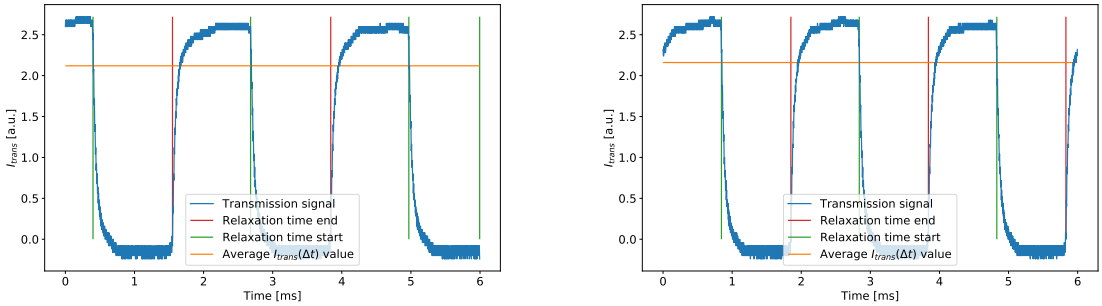

(a) Chopper velocity 9

(b) Chopper velocity 10

Figure 35: Transition signal at all chopper velocities, data part two (as explained in subsubsection 3.2.6). Example description of the plots can be seen in Figure 24.

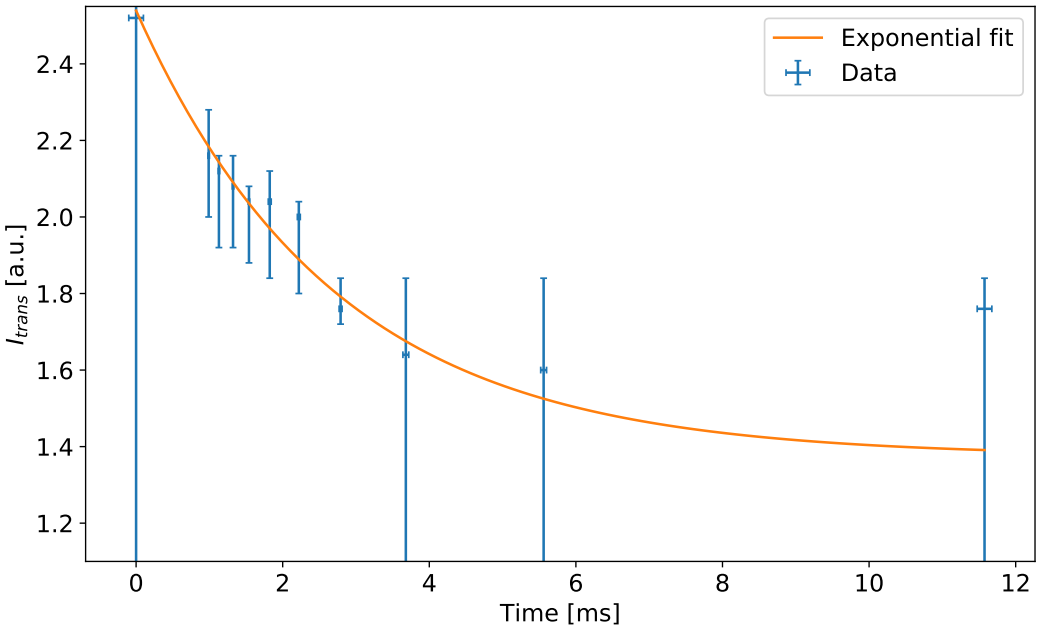

Figure 36: The exponential fit of the Franzen method with a cutted frame. See Figure 25.

Figure 37: Lab notes part 1

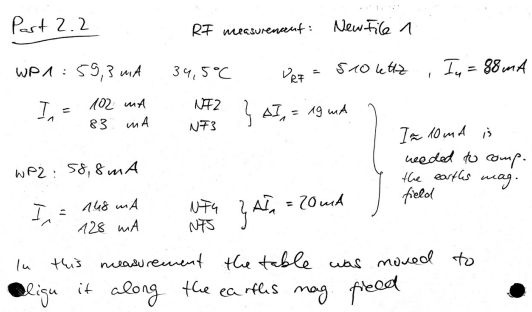

Part 2.2 RF measurement: NewFile 1

WP1: 59,3 mA 34,5 °C ν_{RF} = 510 kHz, I_H = 88 mA

I_1 = 102 mA NF2 } ΔI_1 = 19 mA
83 mA NF3 }

WP2: 58,8 mA

I_1 = 148 mA NF4 } ΔI_1 = 20 mA
128 mA NF5 }

I_1 ≈ 10 mA is needed to comp. the earths mag. field

In this measurement the table was moved to align it along the earths mag field

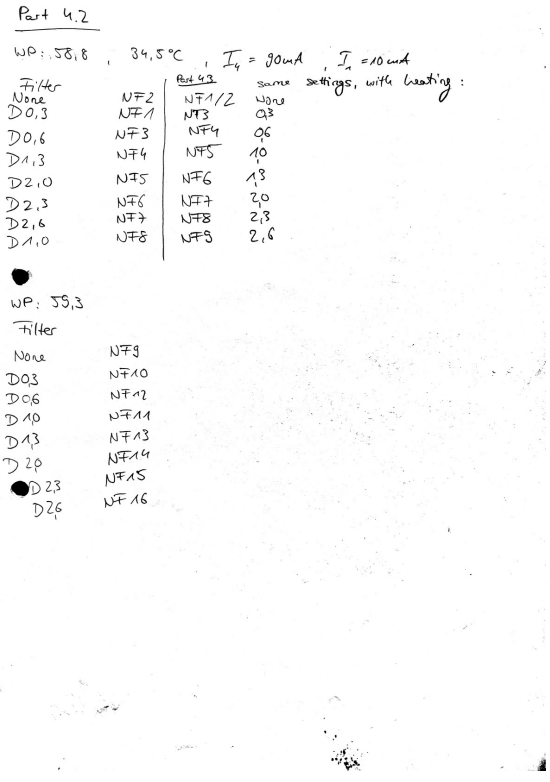

Part 4.2

WP: 58,8, 34,5 °C, I_H = 90 mA, I_1 = 10 mA

Filter		Part 4.3	same settings, with heating:
None	NF2	NF1/2	None
D0,3	NF1	NF3	0,3
D0,6	NF3	NF4	0,6
D1,3	NF4	NF5	1,0
D2,0	NF5	NF6	1,3
D2,3	NF6	NF7	2,0
D2,6	NF7	NF8	2,3
D1,0	NF8	NF9	2,6

WP: 59,3

Filter

None	NF9
D0,3	NF10
D0,6	NF12
D1,0	NF11
D1,3	NF13
D2,0	NF14
D2,3	NF15
D2,6	NF16

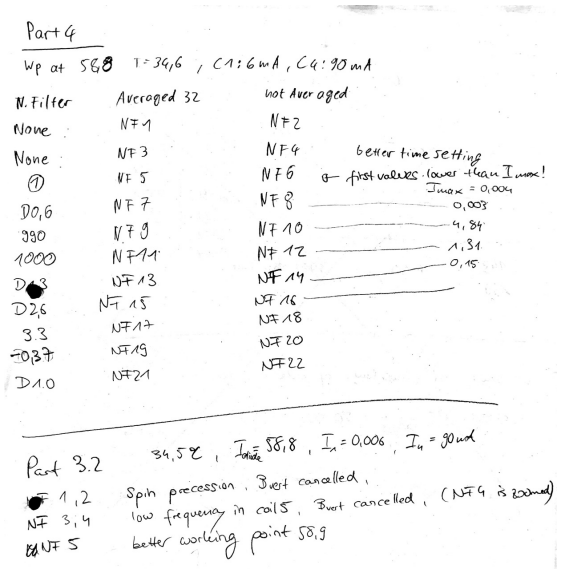

Part 4

Wp at 58,8 T = 34,6, C1: 6 mA, C4: 90 mA

N. Filter	Averaged 32	not Averaged	
None	NF1	NF2	
None	NF3	NF4	better time setting
1	NF5	NF6	← first values lower than I_{max}!
D0,6	NF7	NF8	I_{max} = 0,003
990	NF9	NF10	4,84
1000	NF11	NF12	1,31
D1,3	NF13	NF14	0,15
D2,6	NF15	NF16	
3.3	NF17	NF18	
0,37	NF19	NF20	
D1,0	NF21	NF22	

Part 3.2 34,5 °C, I_{Helm} = 58,8, I_1 = 0,006, I_H = 90 mA

NF 1,2 Spin precession, Burst cancelled,
NF 3,4 low frequency in coil 5, Burst cancelled, (NF4 is zoomed)
NF 5 better working point 58,9

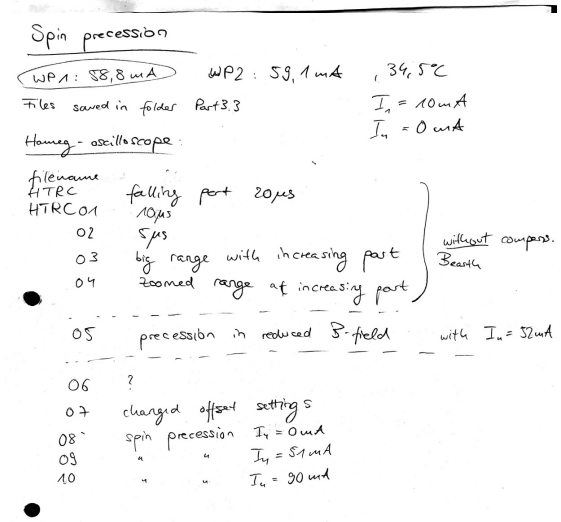

Spin precession

WP1: 58,8 mA WP2: 59,1 mA, 34,5 °C

Files saved in folder Part3.3

I_1 = 10 mA
I_1 = 0 mA

Hameg - oscilloscope:

filename		
HTRC	falling part 20 µs	
HTRC01	10 µs	
02	5 µs	
03	big range with increasing part	without compens. Bearth
04	zoomed range of increasing part	
05	precession in reduced B-field	with I_H = 52 mA
06	?	
07	changed offset settings	
08	spin precession I_1 = 0 mA	
09	" " I_1 = 5,1 mA	
10	" " I_1 = 90 mA	

Figure 38: Lab notes part 2

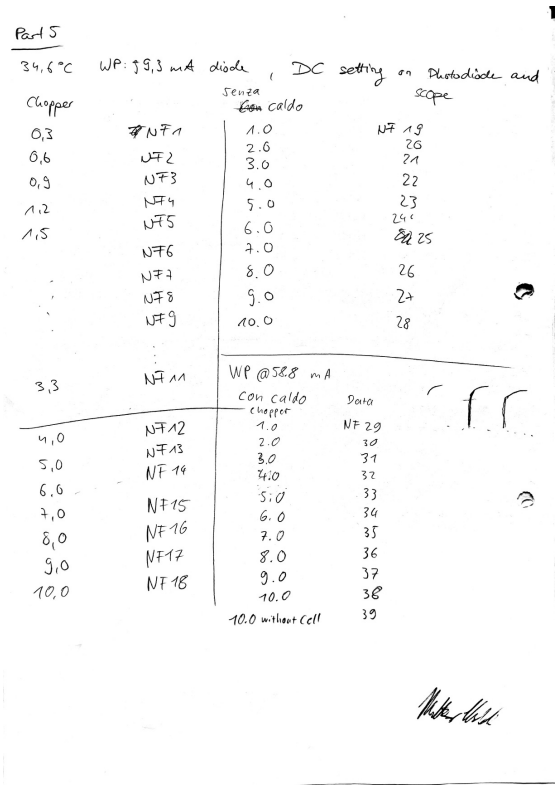

Figure 39: Lab notes part 3